Cell

The developmental basis of fingerprint pattern formation and variation

Graphical abstract

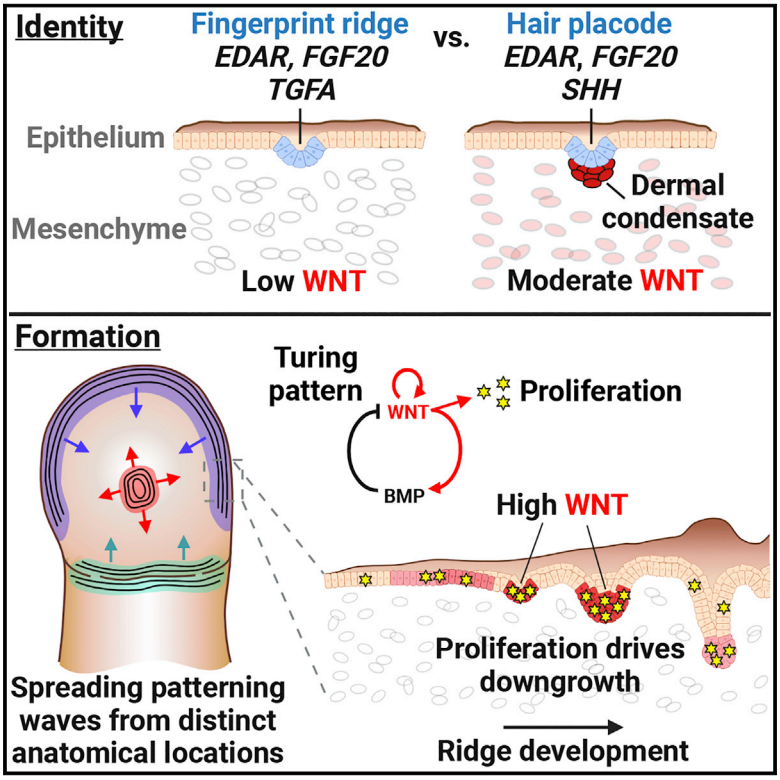

Highlights

- Early fingerprint ridges are epithelial buds molecularly analogous to hair placodes
- Fingerprint ridges do not recruit mesenchymal cells or express late hair follicle markers
- Interacting WNT and BMP signaling defines the spacing interval between ridges
- Ridge initiations from anatomically variable sites determine fingerprint pattern type

Authors

James D. Glover, Zoe R. Sudderick, Barbara Bo-Ju Shih, ..., Yuhang Chen, Michael L. Crichton, Denis J. Headon

Correspondence

denis.headon@roslin.ed.ac.uk

In brief

Signaling pathways that determine formation of human fingerprint ridges.

Glover et al., 2023, Cell *186*, 940–956
March 2, 2023
https://doi.org/10.1016/j.cell.2023.01.015

CellPress

CellPress
OPEN ACCESS

Cell

Article

The developmental basis of fingerprint pattern formation and variation

James D. Glover,[1] Zoe R. Sudderick,[1] Barbara Bo-Ju Shih,[1] Cameron Batho-Samblas,[1] Laura Charlton,[2] Andrew L. Krause,[3] Calum Anderson,[2] Jon Riddell,[1] Adam Balic,[1] Jinxi Li,[4] Václav Klika,[5] Thomas E. Woolley,[6] Eamonn A. Gaffney,[7] Andrea Corsinotti,[8] Richard A. Anderson,[9] Luke J. Johnston,[10] Sara J. Brown,[10] Sijia Wang,[11] Yuhang Chen,[2] Michael L. Crichton,[2] and Denis J. Headon[1,12,*]

[1]The Roslin Institute and R(D)SVS, University of Edinburgh, Edinburgh EH25 9RG, UK
[2]Institute of Mechanical, Process and Energy Engineering, Heriot-Watt University, Edinburgh EH14 4AS, UK
[3]Department of Mathematical Sciences, Durham University, Durham DH1 3LE, UK
[4]State Key Laboratory of Genetic Engineering, Human Phenome Institute, Fudan University, Shanghai 200433, PRC
[5]Department of Mathematics, FNSPE, Czech Technical University in Prague, Prague 16000, Czechia
[6]School of Mathematics, Cardiff University, Cardiff CF24 4AW, UK
[7]Mathematical Institute, University of Oxford, Oxford OX2 6GG, UK
[8]Centre for Regenerative Medicine, Institute for Regeneration and Repair, University of Edinburgh, Edinburgh EH16 4UU, UK
[9]MRC Centre for Reproductive Health, Queens Medical Research Institute, University of Edinburgh, Edinburgh EH16 4TJ, UK
[10]Centre for Genomic & Experimental Medicine, Institute of Genetics and Cancer, University of Edinburgh, Edinburgh EH4 2XU, UK
[11]CAS Key Laboratory of Computational Biology, Shanghai Institute of Nutrition and Health, Chinese Academy of Sciences, Shanghai 200031, PRC
[12]Lead contact
*Correspondence: denis.headon@roslin.ed.ac.uk
https://doi.org/10.1016/j.cell.2023.01.015

SUMMARY

Fingerprints are complex and individually unique patterns in the skin. Established prenatally, the molecular and cellular mechanisms that guide fingerprint ridge formation and their intricate arrangements are unknown. Here we show that fingerprint ridges are epithelial structures that undergo a truncated hair follicle developmental program and fail to recruit a mesenchymal condensate. Their spatial pattern is established by a Turing reaction-diffusion system, based on signaling between EDAR, WNT, and antagonistic BMP pathways. These signals resolve epithelial growth into bands of focalized proliferation under a precociously differentiated suprabasal layer. Ridge formation occurs as a set of waves spreading from variable initiation sites defined by the local signaling environments and anatomical intricacies of the digit, with the propagation and meeting of these waves determining the type of pattern that forms. Relying on a dynamic patterning system triggered at spatially distinct sites generates the characteristic types and unending variation of human fingerprint patterns.

INTRODUCTION

The volar skin of the palms and soles is covered with fine parallel ridges called dermatoglyphs. Prominent in humans and many climbing species, these ridges improve grip[1] and aid in discrimination of texture.[2] On the proximal 2/3rds of the digits, dermatoglyphs are arranged as approximately transverse ridges, but form more complex "fingerprint" patterns at the distal tips (Figure 1A). This pattern is established before birth and maintained throughout life, and has been used for individual identification since the 19th century[3] as well as a diagnostic aid in a number of congenital conditions.[4] The most common types of fingerprint pattern are arch, loop, and whorl (Figure 1A). Arches are the simplest configuration, loops extend to one side of the digit, and whorls have a concentric pattern of ridges at their core. Triradii are Y-shaped formations at which ridges converge at three different angles.[5]

Dermatoglyphs are unique to the volar skin in human. The rest of the body carries hair follicles (HFs), which initiate during embryonic development as circular epithelial placodes upon intensification of expression of EDAR and WNT pathway genes. Each placode then recruits a dermal condensate by emitting an FGF20 signal and undergoes extended tubular downgrowth, driven by SHH signaling.[6]

The human fingerprint pattern is defined by the arrangement of epithelial primary ridges, which form at approximately gestational week 13 on the raised volar pads at the tips of the digits.[7] Over the following weeks, primary ridges form across the rest of the volar skin and, by week 16, sweat glands emerge from the deepest parts of the ridges. Primary ridge formation is

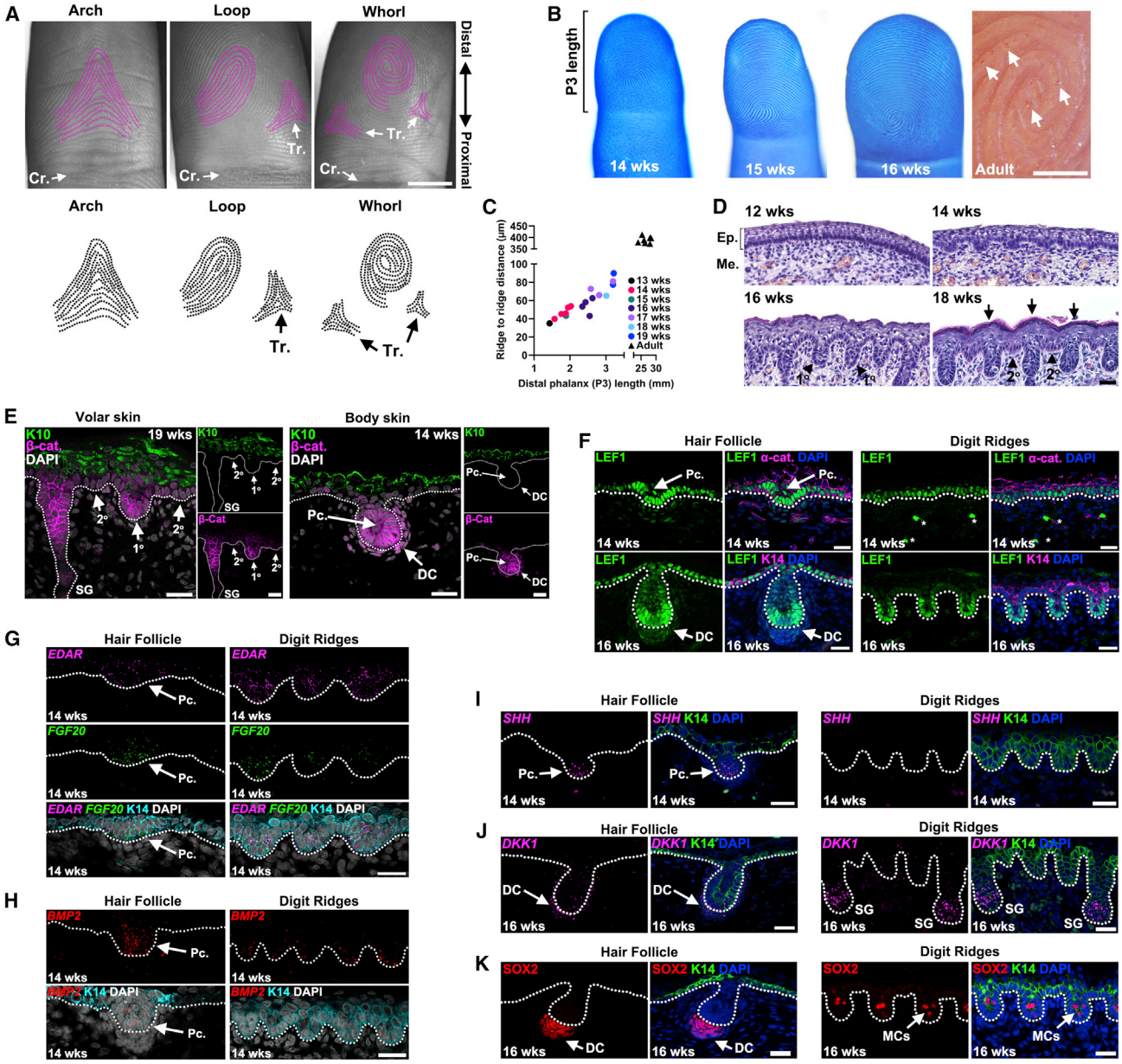

Figure 1. Fingerprint ridge formation and identity

(A) Arch, loop, and whorl patterns on adult fingertips. Tr., triradius; Cr., Crease.

(B) Left: Toluidine blue stain shows fingertip ridge pattern at 14, 15, and 16 weeks estimated gestational age (EGA). Right: Sweat gland pores on the surface of adult fingerprint ridges (arrows).

(C) Ridge to ridge distance (wavelength) and distal phalanx (P3) length at different stages. Each dot represents an individual.

(D) H&E-stained sections of fingertip volar skin from week 12–18 EGA. Arrowheads indicate primary (1°) ridges and secondary (2°) ridges. Arrows indicate skin surface ridges emerging above the primary ridges. Ep., epithelium; Me., mesenchyme.

(E) Left: β-catenin and KERATIN10 (K10) staining of 19 weeks volar skin with sweat gland (SG), 1° and 2° digit ridges. Right: HF primordium on 14 weeks body skin. Pc., placode; DC, dermal condensate.

(F) LEF1 expression in digit ridges and HFs. α-catenin (α-cat.) or KERATIN14 (K14) stain the epidermis.

(G and H) *In situ* hybridization detecting early placode markers *EDAR, FGF20*, and *BMP2* in digit ridges and HF primordia.

(I) *SHH* expression in HF primordia but not digit ridges.

(J) *DKK1* expression in HF and digit ridges.

(K) SOX2 staining, marking the dermal condensate of the HF and Merkel cells (MCs) in digit ridges. Dotted lines indicate epithelial-mesenchymal junctions. Asterisks denote autofluorescent red blood cells. Scale bars, 5 mm (A); 1 mm (B); 25 μm (D–K).

See also Figure S1.

completed by week 17, and smaller secondary ridges then begin to appear between them. The skin surface becomes periodically elevated above the sites of the primary ridges, with each surface corrugation carrying a row of sweat gland pores along its apex.[7,8]

Primary ridges thus define the overall fingerprint configuration, with the selection of arch, loop, or whorl pattern defined by week 15. This selection is influenced by genes that operate early in limb development to exert an indirect effect on fingerprint pattern through their effects on digit length proportions and on the size and shape of the raised volar pads[9] that are present from gestational weeks 9–15.[10] However, the mechanism that governs the pattern and morphogenesis of the primary ridges is not known. Several theories based on pre-existing templates, intercellular signaling, or simple mechanical deformation of epithelium have been proposed.[11,12] Here we show that fingerprint ridges undergo a truncated HF developmental program and that their pattern is produced by a Turing reaction-diffusion system operating in several spreading waves, triggered at distinct initiation sites. The confluences of patterning waves initiated at these variable sites determines the fingerprint pattern type, which together with the inherent randomness of Turing systems delivers an individual uniqueness to each fingerprint.

RESULTS

Fingerprint primary ridges undergo truncated hair placode development

Primary ridges typically form at the center and apex of the distal phalanx (P3) and expand across the skin (Figure 1B). The spacing between the ridges increases linearly from their first appearance, demonstrating that ridge location is fixed as they are laid out and that their pattern is stretched by ongoing digit elongation, with no new primary ridges being inserted between existing ones (Figures 1C and 1D). By week 17, the primary ridges carry periodic downgrowths of sweat glands and become flanked by smaller secondary ridges, with suprabasal thickening above the primary ridges resulting in corrugation of the skin surface. While the primary ridges, like developing HFs, strongly express β-catenin and undergo substantial downgrowth, the secondary ridges do not (Figure 1E), suggesting that their identity is distinct from that of the primary ridges. LEF1, a key transducer and target of WNT signaling,[13,14] is upregulated in the primary ridges and HFs as they develop, demonstrating intensified epithelial WNT signaling in these structures (Figures 1F and S1A). However, mesenchymal LEF1 expression is greatly reduced in volar skin compared with the back skin, where it is present throughout the upper dermis and upregulated in the dermal condensate (Figure 1F).

We find that primary digit ridges express *EDAR*, *FGF20*, and *BMP2*, early markers of HF placodes (Figures 1G, 1H, and S1B), but not the definitive HF marker *SHH*[6] (Figures 1I and S1C). *EDAR* expression in ventral digit epithelium changes from a uniform distribution at week 12 to a punctate pattern through weeks 13 and 14 (Figure S1B), with expression always higher than in the dorsal digit epithelium. The developing HF's mesenchymal component is marked by expression of SOX2 at its core and DKK1 at the periphery,[6] but neither is expressed in the mesenchyme adjacent to primary ridges, nor is there any cell clustering at their base (Figures 1J and 1K). SOX2 also marks the mechanosensory Merkel cells of the ridge epithelium (Figure 1K), as does KERATIN8 (Figure S1D). Thus, the primary ridges have the morphology and molecular characteristics of the early epithelial component of the HF but lack the later drivers of extended downgrowth and dermal condensate that confer HF identity.

In mouse, formation of a dermal condensate by hair placodes is achieved by FGF20-driven recruitment of underlying WNT-stimulated mesenchymal cells.[13,15,16] In human fetal development, LEF1 is present at low levels in ventral limb mesenchyme across the timecourse of fingerprint ridge formation, unlike its higher expression in HF forming skin (Figures 1F and S1A), suggesting that an unresponsive mesenchyme is the basis for lack of dermal condensate formation under the FGF20-positive ridges in volar skin. We assessed the effects of FGF20 and WNT/β-catenin signaling on cultured 12 weeks human embryonic fibroblasts, finding that fibroblasts, regardless of anatomical origin, undergo migration in all signaling conditions, but that FGF20 promotes mesenchymal cell adhesion in a WNT/β-catenin dependent manner (Figure S1F–S1M). This supports the absence of dermal condensates in volar skin resulting from a lack of WNT/β-catenin signaling in the mesenchymal compartment.

Single cell expression profiling delineates shared early but distinct late events in hair follicle and dermatoglyph ridge formation

To permit comprehensive characterization of gene expression during human primary ridge and HF formation, we performed single nucleus RNA-sequencing (snRNA-seq) from week 14 skin of the ridge-forming ventral digit, the sparsely haired dorsal digit, and the back replete with HF primordia. Analysis identified cell clusters (Figure 2A) that cover the cell types expected to be present in developing skin (Table S1). We focused on the basal epithelial keratinocytes and mesenchymal fibroblasts (Figure 2B) as cell types that define tissue structure and ridge formation. Within the epithelium, we identified three subclusters of suprabasal cells: a *KRT14*+ve, *KRT10*+ve population that is prominent on the volar skin (SKI); a more differentiated *KRT10*+ve, *KRT14*-ve population (SKII); and the most superficial keratinocyte layer (SKIII), expressing terminal differentiation markers *IVL* and *FLG*. The basal keratinocytes subclustered into two populations: BKI, which expresses moderate levels of *EDAR*, *FGF20*, *BMP2*, and WNT ligands/receptors; and the ridge/hair placode population BKII, with intensified expression of these genes (Figure 2C). In back skin, BKII also expresses hair placode markers *SHH* and *LHX2*. The basal epithelium expresses *SMARCAD1* (Figures 2C and S1E), a chromatin regulator absolutely required for fingerprint formation (OMIM 129200).[17]

Mesenchyme cluster FbI lies adjacent to the epithelium, based on its high expression of *AXIN2*, *TWIST1*, *TWIST2*, and *APCDD1* (Figure 2C), and in the back skin contains cells expressing *BMP7*, *SOX2*, and *PTCH1* (Figure 2C), markers of dermal condensate identity in mouse.[6] Population FbII is similar to FbI but does not express dermal condensate markers, FbIII expresses markers of both upper and lower mesenchyme, and

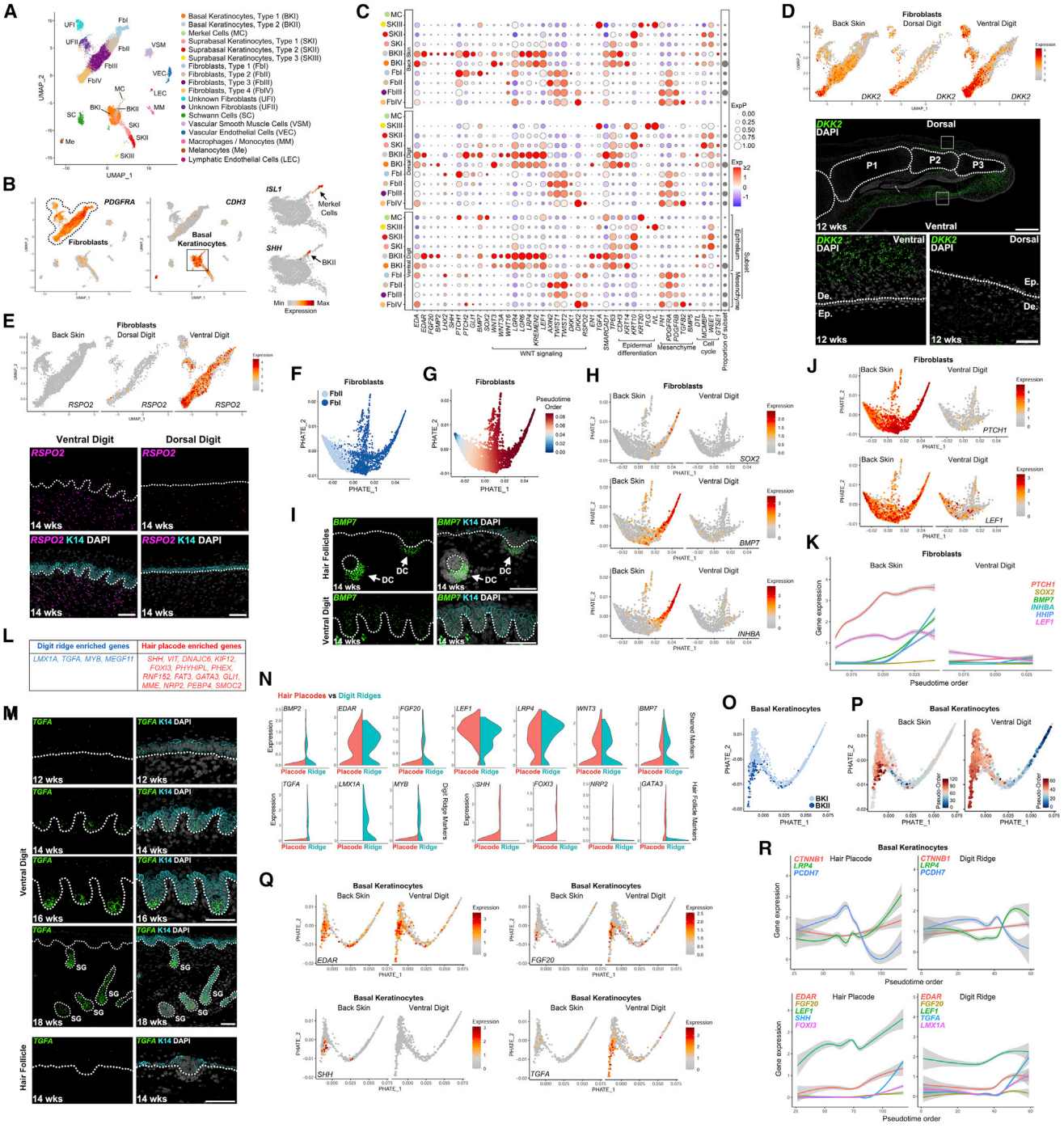

Figure 2. Single nucleus transcriptome profiling of developing human skin

(A) Unbiased clustering of RNA-sequence data from 20,212 nuclei from week 14 ventral digit, dorsal digit, and back skin.

(B) Feature plots of signature genes identifying fibroblast, basal keratinocyte, Merkel cell, and HF placode populations within basal keratinocytes (square).

(C) Dotplot of selected transcript abundance in epithelial and mesenchymal populations of back, dorsal digit, and ventral digit skin. Gray dots (right) indicate proportion of each cell type in the sample. Merkel cells (MC) are identified only in ventral digit skin.

(D) Above: Feature plots of *DKK2* in fibroblasts from different anatomical sites. Below: Expression of *DKK2* in digit mesenchyme at 12 weeks. Individual phalanges are labeled P1-3, from proximal to distal.

(E) Above: Feature plots of *RSPO2* in fibroblast populations from different anatomical sites. Below: Expression of *RSPO2* in ventral and dorsal digit skin.

(F) PHATE map of fibroblast clusters FbI and FbII.

(G) PHATE map from (F) with pseudotime order.

(legend continued on next page)

FbIV is distinguished by its high expression of the WNT inhibitor *DKK2* and its prominence in the volar skin (Figure 2C).

We find that ventral digit mesenchyme has both a greater fibroblast population expressing *DKK2*, and expression of this gene within these cells is also higher, confirmed by *in situ* hybridization (Figure 2D). In mouse, *DKK2* is selectively expressed in volar mesenchyme, where it suppresses WNT signaling and HF formation.[18] Human volar mesenchyme also expresses high levels of *RSPO2*, which is largely absent from back and dorsal digit skin (Figure 2E). RSPO2 is a secreted enhancer of WNT signaling that acts through LGR proteins, which we find expressed at high levels in volar basal epithelium (Figure 2C) representing a potential stimulator of epithelial WNT activity in this skin. A role for *RSPO2* in fingerprint formation is also supported by association of variants at this gene with human fingerprint type.[9]

To understand the basis for failure of dermal condensate formation in volar skin, we analyzed FbI and FbII from back skin and ventral digit skin (Figure 2F). Pseudotime ordering revealed that a dermal condensate trajectory, identified by the expression of *SOX2*, *BMP7*, and *INHBA*, was only present in the haired back skin (Figures 2G and 2H). We validated *BMP7* as a marker of human dermal condensates, finding it also prominently expressed in volar ridge epithelium (Figures 2C and 2I). Recently, mammalian dermal condensate cell fate determination was found to be dependent on combined SHH and WNT signaling in the mesenchyme.[13,19] Consistent with a lack of epithelial *SHH* expression and low mesenchymal WNT activity in the ventral digit, we only observed high expression of *PTCH1* (a Hedgehog pathway target gene) and *LEF1* in the back skin mesenchyme (Figures 2J and 2K). Expression of these genes increases along the pseudotime order and precedes the expression of definitive dermal condensate marker genes *SOX2*, *BMP7*, and *HHIP* in back skin fibroblasts (Figure 2K). No such expression changes were seen in ventral digit fibroblasts, indicating that a dermal condensate fate trajectory is not initiated in the volar mesenchyme.

To identify the differences in their epithelial components, we compared expression profiles between digit ridges and HF placodes. This approach identifies a suite of pan-epithelial appendage upregulated genes, but also genes unique to each appendage type (Figure 2L). In ventral digit skin, this included *TGFA*, encoding the epithelial mitogen TGFα,[20] and in the back, *SHH* was the top gene enriched in the HF placode. Other known markers of hair placodes, including *FOXI3* and *NRP2*,[21,22] were enriched only in the back skin BKII population. We detect low *TGFA* expression in unpatterned volar skin, becoming abundant in ridges as they emerge and still more strongly expressed in sweat glands as these bud off and grow down from the primary ridges (Figure 2M). On the back skin, only low levels of *TGFA* are associated with HF initiation (Figure 2M). Thus, *TGFA* is a selective marker associated with ridge and sweat gland, but not HF, emergence and growth.

Digit ridges and HF placodes express many genes in common, while each also has a set of specific upregulated genes (Figure 2N). To understand this phenomenon, we performed trajectory analysis of the back skin and ventral digit basal keratinocyte populations (Figures 2O and 2P), finding a common upregulation of *EDAR* and genes involved in the WNT signaling pathway, including *CTNNB1*, *LEF1*, and *LRP4*, along the pseudotime order toward HF placode or digit ridge (Figures 2Q and 2R). These common expression changes precede the genes unique to each appendage type, such as *TGFA* or *SHH*, which are upregulated later in the trajectory. This demonstrates an early commonality of epithelial appendage trajectories followed by distinct later states, notably defined by expression of different mitogens.

Fingerprint ridges are produced by banded proliferation

Prior to ridge emergence, volar epithelium undergoes accelerated maturation compared to dorsal digit and body skin, indicated by its sequence of keratin expression and stratification (Figures 3A, S2A, and S2B). A continuous KERATIN14 (K14)+ve intermediate layer appears on ventral digit epithelium by week 13 (Figure 3A), with ridge formation often closely following, but never preceding, this event. Isolated suprabasal K14+ve cells appear on other body sites, but only form a coherent layer on volar skin (Figures 3A and S2B), consistent with the greatest proportion of cluster SKI being detected in the ventral digit epithelium (Figure 2C).

Though the proliferative fraction of basal cells in volar epidermis is not greater than on other body sites, by week 12, a densely packed and columnar basal layer is present in the ventral digit skin (Figures 3A–3C and S2C–S2E). By week 17, basal epidermal density and cell shape on the dorsal digit are similar to that of the 13 weeks ventral digit (Figures 3B and S2C).

Mechanical deformation of an overcrowded epithelium has been proposed as a driver for periodic ridge formation through a buckling mechanism.[23] Although the ventral digit has a higher basal cell density than dorsal digit and body skin (Figures 3C, S2C, and S2D), we did not find any indication of directional strain

(H) Feature plots of back skin and ventral digit fibroblasts for the dermal condensate markers *SOX2, BMP7*, and *INHBA* on the PHATE map.
(I) *BMP7* expression in back skin HFs and in digit ridges. DC, dermal condensate.
(J) Feature plots of *PTCH1* and *LEF1* in back skin and ventral digit fibroblasts.
(K) Expression levels of indicated genes across pseudotime order toward dermal condensate.
(L) Table of genes selective for digit ridge or hair placode upregulation.
(M) Expression of *TGFA* in ventral digit and back skin HFs.
(N) Violin plots comparing gene expression between BKII populations of the back skin and ventral digit samples.
(O) PHATE map of basal keratinocyte populations BKI and BKII.
(P) PHATE maps of BKI and BKII with projected pseudotime order of back skin and ventral digit nuclei.
(Q) Feature plots of back skin and ventral digit basal keratinocytes for shared (*EDAR*, *FGF20)* and specific (*SHH*, *TGFA*) BKII genes.
(R) Expression levels of indicated genes across pseudotime order for back and ventral digit basal keratinocytes toward hair placode or digit ridge identity. Scale bars, 500 μm (D, middle); 50 μm (D lower, E lower, I, and M).
See also Figure S1.

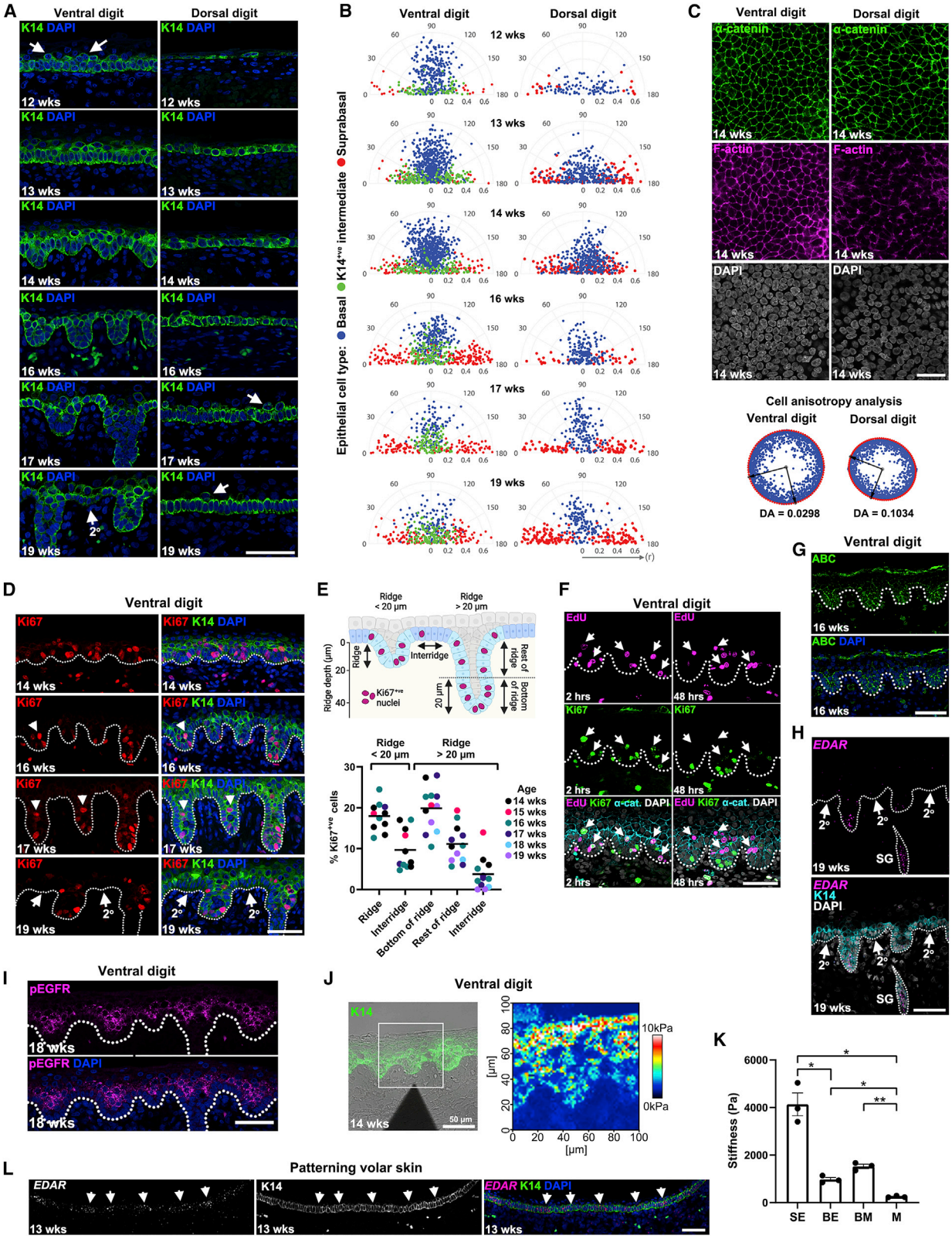

(legend on next page)

in volar epithelium where ridge formation is imminent (Figures 3C and S2F). We also assessed YAP activity as an indicator of cellular mechanosensing,[24] but did not observe heterogeneities in its activity accompanying initial ridge formation. Only after their establishment do digit ridges exhibit higher YAP signal than their surrounding epithelium, as do HF primordia (Figures S2G–S2I). In addition, we did not identify arrangements of Merkel cells or underlying dermal structures that could represent an external template for primary ridge pattern (Figure S3). These results indicate that the pattern of ridges is produced autonomously within the epithelium, but not through simple cell overcrowding and consequent deformation.

We assessed cell proliferation in volar epithelium, finding Ki67+ve nuclei at high frequency within ridges as they emerge and little proliferation in interridge epithelium (Figures 3D and 3E). As ridges downgrow, their deepest portion maintains the greatest proliferation, while the intermediate region, including the suprabasal cells of the ridge core, proliferates at a lower rate (Figures 3D and 3E). Pulsing of cultured volar skin with EdU confirmed that the ridge bases are the zone of highest proliferation, while chasing of this label revealed that EdU+ve cells are displaced suprabasally as ridges downgrow (Figure 3F). The deepest part of the ridges displays highest WNT/β-catenin activity and retains *EDAR* and LEF1 expression throughout their proliferative downgrowth (Figures 3G, 3H, S1A, and S1B). The proliferative suprabasal core of the ridges displays active EGFR signaling (Figure 3I), potentially contributed to by production of its ligand, TGFα, by ridge basal cells. These observations implicate localized proliferation as the process responsible for producing ridge downgrowths. Once full ridge depth is attained, ongoing proliferation (Figure 3D) drives sweat gland downgrowth and thickening of the suprabasal layer to produce the surface corrugations (Figure S2A). Consistent with their lack of *EDAR*, *FGF20*, and LEF1 expression (Figures 3H, S1A, and S1B), we did not observe proliferation in secondary ridges (Figure 3D).

To understand whether differences in proliferation on the basal epithelium could promote morphological ridge formation, we assessed the mechanical structure of developing skin using atomic force microscopy. Focal proliferation can lead to the emergence of U-shaped buds in stratified epithelia under appropriate physical conditions of a soft proliferative layer and mesenchyme below a rigid suprabasal layer, forming a gradient of stiffness.[25] Addressing whether these conditions are met in embryonic ventral digit skin, we found that the basal epithelium, K14+ve intermediate layer and mesenchyme are soft, while the thick K10+ve suprabasal epithelial layer is stiffer, as is the thin basement membrane (Figures 3J, 3K, and S2J). Meeting this condition of a soft proliferative basal epithelium under a stiffer overlying suprabasal canopy is sufficient to explain ridge downgrowth in the volar epithelium.

EDAR and WNT signaling drive proliferation in a range of epithelia,[26–28] suggesting that heterogeneity in their expression could be responsible for partitioning the epithelium into ridges and interridges. *EDAR* is expressed throughout the early basal epithelium, before becoming localized at weeks 13 and 14 to the nascent ridges (Figure S1B) and diminishing in interridges. In areas about to undergo ridge formation, we detect periodically patterned *EDAR* expression prior to epithelial corrugation (Figures 3L and S1B). For unbiased assessment of pattern, we used wavelet analysis, which supported the detection of prepatterned *EDAR* expression at the appropriate wavelength for fingerprint ridges before structural alteration of the epithelium (Figure S2K). Thus the symmetry-breaking event in the volar epithelium is a change in gene expression, as it is for HFs on the body.[15] This partitions the epithelium into bands of high and low proliferation, the former corresponding to the sites of high EDAR expression and WNT activity. This occurs in the highly specialized structure of the volar skin, which is established just prior to ridge formation and primed to enforce downgrowth of intensely proliferative foci.

WNT and EDAR signaling drive ridge formation and patterning

Localized *EDAR* expression prefigures primary ridge locations, as it does for HFs.[29] The spatial patterning of HFs is guided by a Turing reaction-diffusion system, with EDAR and WNT/β-catenin signaling intertwined to activate[30] and BMP to inhibit[31,32] HF specification in naive epidermis. Loss of function of EDAR, or its ligand EDA, causes hypohidrotic ectodermal dysplasia (OMIM 305100), characterized by defects in hair, tooth, and gland

Figure 3. Primary ridges undergo proliferative downgrowth specified by a molecular pre-pattern

(A) K14 expression in ventral and dorsal digit epithelium. Arrows indicate suprabasal K14+ve cells in the early ventral digit and the later dorsal digit epithelium.

(B) Quantification of epithelial cell shape in basal (blue), K14+ve intermediate (green) and suprabasal (red) compartments. Each dot represents a single cell, plotted in polar coordinates indicating their orientation (θ, 0°/180° relative to basal plane = left/right; apical = 90°) and stretch (r).

(C) Above: z stack projection of ventral and dorsal digit basal epidermis stained to detect F-Actin, α-catenin and with DAPI. Below: Quantification of degree of anisotropy (DA) of basal epithelial cell shape for samples above. Directional distortion is not detected.

(D) Ki67 detection in ventral digit.

(E) Above: schematic of the distinct regions of the epithelium and ridges quantified. Below: quantification of proliferation in different compartments of primary ridges. Each dot represents an individual sample.

(F) EdU pulse-chase of cultured 16 weeks ventral digit skin at 2 and 48 h, co-stained for Ki67.

(G) Active β-catenin staining in digit ridges.

(H) *EDAR* expression in sweat glands but not secondary ridges at week 19.

(I) Immunofluorescent detection of phospho-EGFR in suprabasal cells of ridges.

(J) Stiffness of ventral digit skin components assessed by atomic force microscopy. K14 marks epidermis (left). Corresponding force map of highlighted area (right).

(K) Stiffness of different structures in week 14 volar skin. SE, suprabasal epithelium; BE, basal epithelium; BM, basement membrane; M, mesenchyme. Error bars represent SEM from three independent samples. *$p < 0.05$; **$p < 0.01$ = ANOVA with pairwise comparison.

(L) Periodic *EDAR* expression in week 13 volar skin, prior to ridge emergence. Dotted lines indicate epithelial-mesenchymal junctions. Scale bars, 50 μm.

See also Figures S2 and S3.

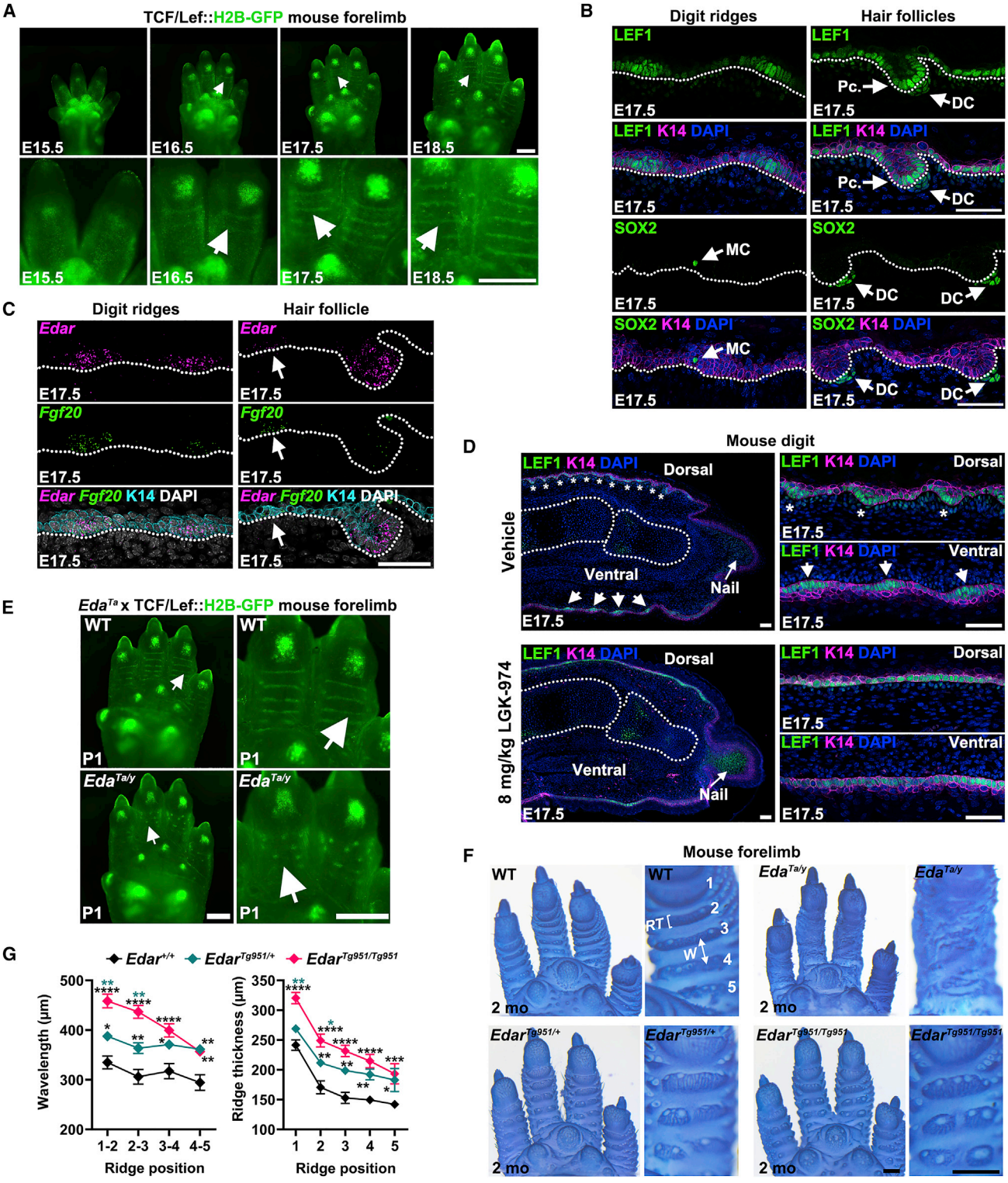

Figure 4. WNT and EDAR signaling define digit ridge pattern in mouse

(A) Emergence of transverse digit ridge (arrows) pattern in mouse development, visualized by the WNT reporter TCF/Lef::H2B-GFP.

(B) Above: LEF1 expression in mouse digit ridges and HFs at E17.5. Below: SOX2 marks the dermal condensate (DC) in HFs and the Merkel cells (MC) in digit ridges (arrows).

(C) Expression of *Edar* and *Fgf20* in mouse digit ridges and dorsal digit HFs at E17.5. Arrow indicates *Edar* and *Fgf20* in nascent hair placode.

(legend continued on next page)

formation and by diminished and indecipherable fingerprint patterns.[33,34]

In mice, transverse digital ridges represent the closest structure to human fingerprint ridges.[9] Arising at the distal end of the digit, these ridges display elevated WNT signaling, and their formation progresses proximally along the digit over two days (Figure 4A). As in human, mouse transverse ridges contain Merkel cells, do not recruit a dermal condensate (Figure 4B), and display expression of *Edar* and *Fgf20* both within ridges and at sites that precede their formation (Figures 4C and S4A–S4C). Mouse ridges do not express *Shh* (Figure S4E), but, as in human, *Tgfa* is detected in these ridges and in sweat gland rudiments (Figures S4F and S4G).

We find that diminished function of the sole TGFα receptor, EGFR, in mouse is associated with reduced sweat gland formation and modest effects on ridge shape, but not on overall ridge arrangement (Figures S4H–S4K), consistent with TGFα representing an output of the core patterning system that drives further ridge and gland morphogenesis.

Inhibition of active WNT secretion from embryonic day 15.5 (E15.5) to E17.5 abolishes digit ridge formation, demonstrating the requirement for WNT signaling in their development, as for the development of HFs (Figures 4D, S4L, and S4M). Ablation of EDAR signaling using the Eda^{Ta} mutant line causes production of a spotted rather than a striped pattern (Figure 4E), while increasing EDAR signaling[35] causes thicker, more widely spaced, ridges to form (Figures 4F and 4G). Such stripe-to-spot transitions and coordinated tuning of ridge size and spacing are hallmarks of Turing patterning systems.[36,37] Thus, EDAR is required for normal ridge patterning, and its effects on the size, spacing, and shape of the digit ridges indicate the operation of a Turing reaction-diffusion system in defining their arrangement.

BMP antagonises WNT-induced digit ridge formation

During HF formation, EDAR signaling is regulated by and cooperates with the WNT/β-catenin pathway[30] and is antagonistically regulated by BMPs.[31,32] *Bmp2* is expressed by HF placodes in mouse[6] and in digit ridges (Figure S4D). We find that BMPs are also expressed in human hair placodes and digit ridges (Figures 1H, 2C, and 2I). In volar skin, the active form of the BMP signal transducer SMAD1/5 is detected broadly throughout ridge and interridge basal epithelium (Figure 5A and S4N), in contrast to hair placodes, in which BMP activity is lower than surrounding epithelium (Figure 5A). Analysis of BMP target gene expression in basal keratinocytes further supports the idea of volar epidermis experiencing higher BMP activity than skin from HF producing regions (Figure 5B). To assess the functional importance of BMP signaling in dermatoglyph development, we inhibited this pathway *in utero* from E15.5 to E17.5. This resulted in the formation of broader ridges, with expanded WNT activity and increased expression of digit ridge marker genes (Figures 5C–5F), similar to the larger HFs produced upon suppression of BMP signaling.[15] Strikingly, BMP inhibition also triggered expression of *Shh* in mouse digit ridges (Figure 5G), demonstrating that BMP signaling in the volar epithelium is responsible for suppressing this key hair placode identity gene in digit ridges.

Epithelial proliferation drives ridge morphogenesis (Figure 3), suggesting that the signaling pathways influencing the ridge pattern should yield a proliferative output. We investigated the effects of WNT and BMP signaling on cell proliferation using a human iPS cell-derived fetal skin organoid system.[38] Based on their expression in the volar skin (Figure 2C), we used recombinant WNT3A + RSPO2 proteins to stimulate WNT signaling and recombinant BMP2 as a representative of the BMP pathway. We find that epidermal proliferation is stimulated by WNT signaling and supressed by BMP treatment (Figures 5H and 5I). WNT-stimulation of proliferation is capable of overcoming BMP inhibition, permitting cell division in an environment that is both WNT+ve and BMP+ve (Figures 5H and 5I). Consistent with these findings, inhibition of WNT signaling also reduced epidermal proliferation (Figures 5H and 5I). Similar effects on proliferation were observed in mouse digit skin when WNT or BMP signaling was modulated (Figure S4O).

To understand how BMP signaling suppresses WNT proliferative responses, we assessed expression of LEF1. In skin organoids WNT3A + RSPO2 treatment increased epithelial LEF1 abundance, whereas BMP treatment strongly suppressed epithelial LEF1 expression (Figure 5J), consistent with BMPs inhibiting epithelial LEF1 in embryonic mouse skin.[39–41]

The observed BMP-driven suppression of WNT response in organoid epithelium fits the requirement for an inhibitor in a Turing reaction-diffusion system. To evaluate WNT stimulation of BMP production, a second key regulatory requirement of Turing systems, we assessed transcriptional responses in WNT-treated *ex vivo* cultured human fetal volar skin. We found that WNT stimulation significantly upregulated expression of *EDAR* and *FGF20*, known WNT target genes in mouse,[16,30] and also *WNT16*, which is highly expressed in volar skin (Figure 2C). Matching Turing system requirements, WNT stimulation also induced *BMP7* expression, though *BMP2* did not significantly increase in this time frame (Figure 5K).

Having defined a set of regulatory interactions fulfilling the core Turing reaction-diffusion system requirements, we simulated such a system to assess its ability to recreate transverse ridge patterns and their experimental variations. In this system,

(D) LEF1 expression in E17.5 vehicle and LGK-974 treated (WNT-suppressed) forelimbs. Arrows indicate digit ridges; asterisks indicate HF primordia.
(E) Eda^{Ta} mutant newborns have WNT-positive spots rather than ridges. Eda^{Ta} is a loss of function.
(F) Digit ridge pattern upon alteration of EDAR signaling. Toluidine blue stained week 8 forelimbs. $Edar^{Tg951}$ is a high copy number line, with heterozygous and homozygous individuals.
(G) Quantification of ridge spacing (wavelength) and ridge thickness in wild type and $Edar^{Tg951}$ transgenic mice. As annotated in (F), ridge position is numbered, and ridge thickness (RT) and interridge wavelength (W) are indicated. Dotted lines indicate epithelial-mesenchymal junctions or outline phalanges. Error bars represent SEM from at least 5 forelimbs analyzed per genotype. *$p < 0.05$; **$p < 0.01$; ***$p < 0.001$; ****$p < 0.0001$ = ANOVA with pairwise comparisons. Scale bars, 500 μm (A, E, F); 50 μm (B–D).
See also Figure S4.

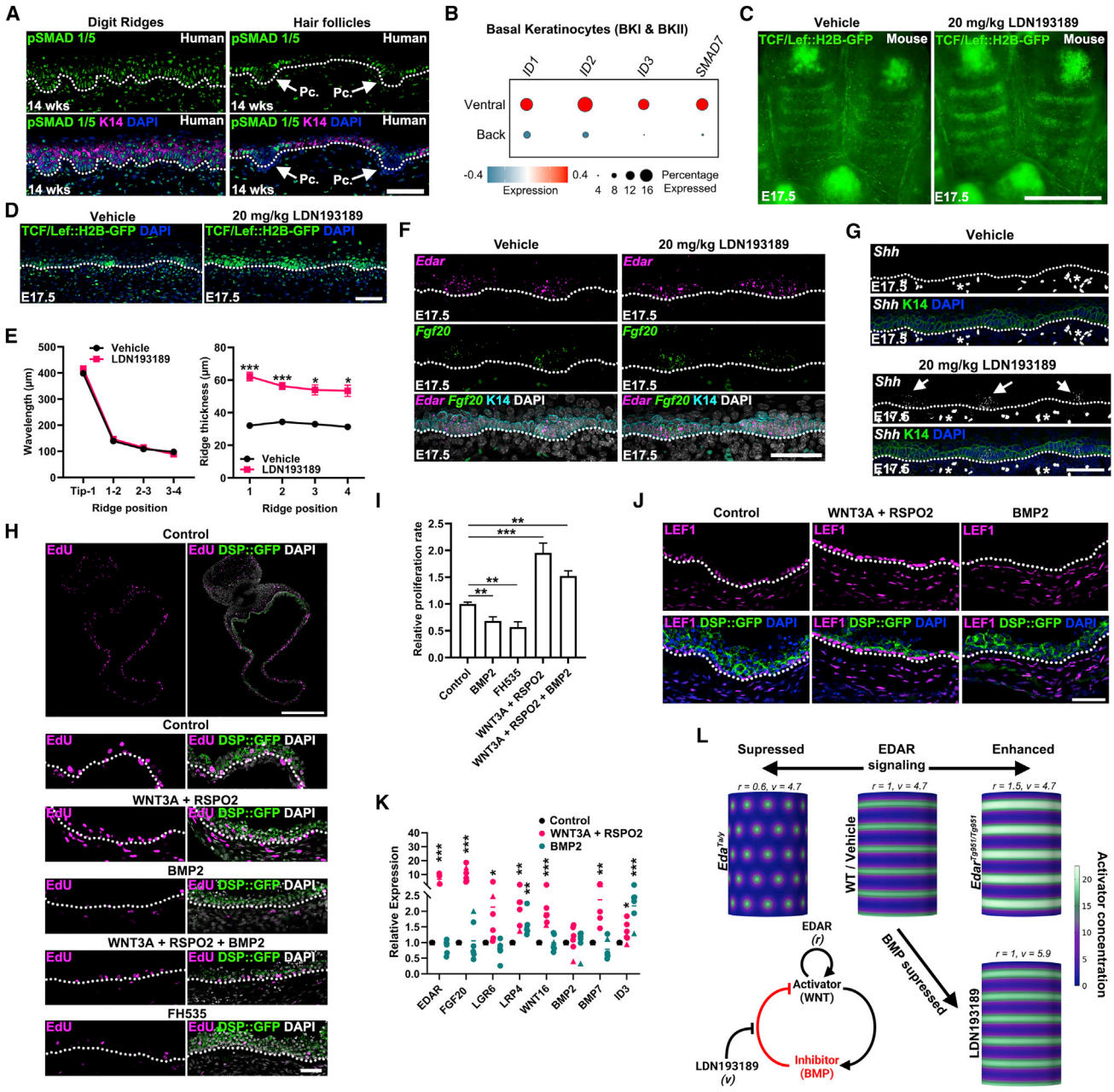

Figure 5. BMP signaling inhibits ridge formation

(A) Phospho-SMAD1/5 immunodetection in digit ridges and HFs.

(B) Dotplot of BMP pathway target gene expression in basal keratinocyte populations in back and ventral digit.

(C) Suppression of BMP signaling *in utero* by treatment with LDN193189 alters transverse ridge pattern in TCF/Lef::H2B-GFP embryos.

(D) Sectioned digit skin showing expanded reporter signal in LDN193189 treated mice.

(E) Quantification of ridge spacing (wavelength) and thickness in vehicle control and LDN193189 treated embryos. Error bars represent SEM; n = 4 per treatment. *p < 0.05; ***p < 0.001. Student's t test.

(F and G) (F) Expression of *Edar* and *Fgf20* and (G) *Shh* in vehicle control and LDN193189 treated transverse ridges.

(H) Day 33 human embryonic skin organoids treated with WNT3A + RSPO2, BMP2, FH535 (WNT inhibitor), or WNT3A + RSPO2 + BMP2. EdU was administered to detect proliferating cells.

(I) Quantification of epithelial proliferation in treated organoids. Error bars represent SEM from at least 5 organoids per condition. *p < 0.05; **p < 0.01; ***p < 0.001. Welch's t-test.

(J) LEF1 expression in organoids treated with WNT3A + RSPO2 or BMP2.

(K) qRT-PCR of developmental transcripts in cultured volar skin samples treated for 24 h with WNT3A + RSPO2 or BMP2. Each point represents an individual piece of skin from digit, palm, or sole from 11 weeks (triangles) or 12 weeks (dots) embryos. *p < 0.05; **p < 0.01; ***p < 0.001. Student's paired t test.

(legend continued on next page)

EDAR tunes activator function, representing epithelial WNT as demonstrated in other systems,[30] and BMPs are inhibitory (Figure 5L). Modulating this simulated network to match experimental alterations of EDAR or BMP signaling replicates the pattern changes observed *in vivo*. Simulation of increased EDAR leads to formation of thicker, more widely spaced stripes, while its suppression causes production of spots. Conversely, modeling suppression of BMP signaling widens the transverse ridges, as observed *in vivo* (Figure 5L). Thus EDAR, WNT, and BMP acting in a reaction-diffusion system are sufficient to explain the production of the parallel ridge patterns, with high WNT signaling serving to drive cellular proliferation and emergence of morphological ridges.

Human fingerprint pattern is determined by variable anatomically defined initiation sites

Before and during fingerprint patterning the fetal hand carries several raised volar pads (Figure S5A). The first primary ridges to emerge are on the palm and volar pads of the digit tips from week 13 (Figures 6A, S3A, S5B, and S5C). Initiation of patterning also occurs at the tip of the digit at the dorsal-ventral boundary, and sometimes on the most proximal phalanx (P1; Figures 6A and S5B), where smaller pads are present.[42] Ridge formation spreads from these initiation sites in waves that cover the palm and digits by week 17, with the medial portion of the digits the last area to acquire ridges (Figure S5B).

We found that LEF1 and *EDAR* expression anticipate the spatial and temporal progression of ridge formation. Expression of these WNT target genes is first observed in the epithelium on the proximal slope of the volar pads on the fingertips (Figures 6B and 6C) at week 10. *FGF20* and *TGFA* are also detected on the volar pad at the site of *EDAR* expression (Figures S1B, S5D and S5E). We found that *RSPO2* expression initiates specifically in the mesenchyme of the volar pads (Figures 6D and S5F), representing a likely contributor to eliciting the WNT pathway activity and patterning gene expression in the immediately overlying epithelium. By week 13, *EDAR* and LEF1 expression have spread across the pad toward the distal tip and proximally to the medial and proximal phalanges, with sharp expression boundaries at the nail bed and dorsal-ventral boundary of digit skin (Figures 6E, 6F, S5E, and S5G). On the ventral digit, the expression of mesenchymal *DKK1*, a WNT pathway inhibitor, is reciprocal to that of *EDAR* and LEF1 (Figure 6G) when ridge formation begins, being largely confined to the medial portion. In addition to the ridge patterning genes (Figures 6B–6E and S5H), a wave of K14 expression also spreads proximally from the distal tip along the length of the digits (Figures S5D and S5E), starting from week 10. Thus, molecular waves of WNT activity and skin differentiation precede the spreading zones of ridge emergence.

The volar skin carries a series of flexion creases (Figures 6H, 6I, and S6A), which form across the palm and digit from week 8, with distal digit creases forming later than the palm-digit and major palm creases.[42] Toward the digit tip, a third site of ridge initiation lies adjacent to the distal interphalangeal crease, with primary ridges here usually arising later than the patterning waves emerging on the volar pad and at the distal tip, and typically in parallel with the crease itself (Figures 6A, 6H, S5B and S5I, and S6B). Early forming creases strongly suppress overt primary ridge formation within themselves, though throughout the timecourse of ridge formation *EDAR*, *FGF20*, and *BMP2* expression is maintained across the creases in the absence of morphologically apparent ridges (Figures 6J and S6C–S6H). This demonstrates that crease epithelium remains competent to undergo patterning, but that ridge formation is inhibited by a mechanism other than impaired cell signaling. Epithelial proliferation within creases matches or exceeds that of the primary ridges (Figures 6K and S6C) although the suprabasal layer is severely reduced at these sites (Figures 6I, S6O, and S6P), pointing to the mechanical environment causing changes in epithelial dynamics and post-mitotic distribution of cells. This is reflected in the broader, misshapen ridges immediately adjacent to the center of the crease (Figures 6I and 6L). Merkel cells populate definitive primary ridges soon after their formation but remain scattered across the creases (Figures S6I and S6J), illustrating that creases have an incomplete or unstable ridge identity, further supported by their expression of *TGFA* (Figure S6G). Structurally, crease articulation sites are characterized by normal epidermal polarity and organization but a very thin suprabasal layer (Figures 6I and S6K–S6P). This, together with their dynamic movements, rather than absence of appropriate gene expression, suppresses morphological ridge formation at these sites.

Flexion creases often compartmentalize ridge patterns such that zones with coherent ridge orientations are interrupted by parallel alignments of the crease-proximal ridges (Figures 6H and S6B). In areas such as the fingertip, where independent waves of ridge formation are unimpeded by creases and free to meet, the collision of three waves terminates in formation of a triradius (Figures 6M and 6N). To assess the relevance of these distinct initiating waves and anatomical landmarks on fingerprint pattern, we simulated the operation of a Turing reaction-diffusion system across a field with properties matching those of the fingertip. This simulated field encompasses the dorsal-ventral expression boundary and the volar pad initiation of *EDAR* and LEF1 expression, and the instability imposed by partial ridge identity within the interphalangeal crease. By altering the relative timing, location, and angle of these initiation sites, we could faithfully reproduce the major pattern types of arch, loop, and whorl (Figure 6O), and the rarer patterns of ridge dissociation and "ridges-off-the-end."[43] Thus the operation of a simple patterning system that reads distal limb geometry to trigger initiation events, and the subsequent collision of spreading patterning waves, is capable of generating the many different types of human fingerprint pattern.

(L) Schematic of molecular interactions defining transverse ridge pattern. Parameters *r* and *v* influence Activator production and strength of Inhibitor's suppression of the Activator, respectively. Outcomes of simulations of digit ridge patterning upon reduction or augmentation of EDAR signaling, and by suppression of BMP signaling. Dotted lines indicate epithelial-mesenchymal junctions. Asterisks denote autofluorescent blood cells. Scale bars, 50 μm (A, D, F, G, H lower, and J); 500 μm (C, H top).
See also Figure S4.

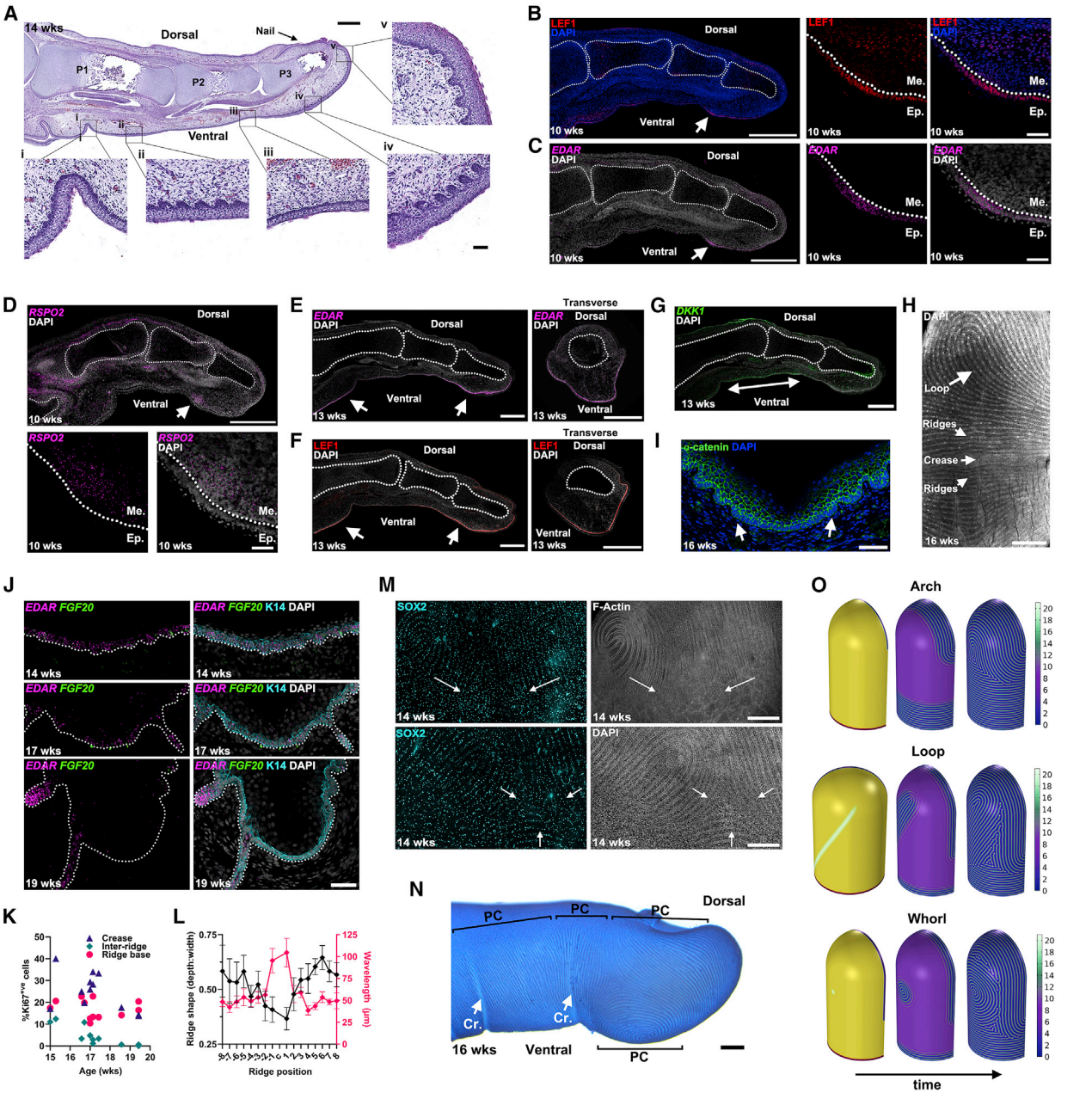

(legend on next page)

DISCUSSION

We report that fingerprint ridges are epithelial appendages, structurally and molecularly resembling HF and tooth primordia,[44] though lacking their mesenchymal components and extended downgrowth (Figure 6P). The changes that dermatoglyph patterns undergo upon modulating intercellular signaling, including stripe-spot transitions and coordinate changes to ridge size and spacing, identifies their formation as underlain by a Turing reaction-diffusion system.[36,45] Such systems drive spatial patterning by amplifying inhomogeneities, either from random molecular noise or discontinuities at tissue boundaries, and readily propagate as a wave away from the initial sites of pattern emergence.[46] Within this system, experimental alterations to the patterns and regulatory interactions identify WNT and EDAR as activatory inputs and BMPs as inhibitory, similar to the system that arranges HFs across the rest of the skin.[6,15,30] Although BMPs fulfill the criteria required for inhibitors in this system, and snRNA-seq did not detect other diffusible WNT inhibitors expressed in digit ridges, we cannot exclude the possibility that other factors known to inhibit epithelial WNT/β-catenin activity, including FGF20,[15,16] could also contribute to the inhibitory function. Modeling of these interactions shows that they can explain human and mouse dermatoglyph patterns and their variation. This system leads to upregulation of TGFα, an EGF receptor ligand,[20] at the base of the ridges. TGFα thus represents an output of the ridge patterning system, driving further ridge morphogenesis and promoting sweat gland emergence at periodic intervals along each ridge. This activity of TGFα mirrors that of SHH in HFs, where it promotes morphogenesis and extended epithelial downgrowth.[6] The role of the TGFα-EGFR pathway in promoting sweat gland formation is in sharp distinction to the inhibitory effect of EGFR signaling on hair placode formation[47] and may be useful to aid restoration of sweat gland development in hypohidrotic ectodermal dysplasias.[48]

Dermatoglyph primary ridges are entirely epithelial structures despite their expression of *FGF20*, a key epithelial recruitment factor for mesenchymal cell condensation under hair placodes.[16] Volar mesenchyme experiences little WNT activity, which is required for competence to form a dermal condensate[13] and for aggregation responses to FGF20 signals. This low WNT activity may be contributed to by the elevated expression of *DKK2* in ventral digit mesenchyme, as ablation of DKK2 in mouse causes HF formation in the volar skin,[18] though in mouse, the expression of *DKK2* is observed in mesenchyme adjacent to the epithelium, while expression in human is stronger in the deeper mesenchyme. High levels of BMP signaling and the intensified expression of the transcription factor ENGRAILED1[49,50] that we identify in dermatoglyph ridges may also contribute to suppression of HF formation in volar skin, including through repression of *SHH* expression. Hedgehog signaling has recently been shown to act on WNT-stimulated mesenchyme to promote dermal condensate cell fate acquisition,[19] suggesting that multiple intersecting signals required for dermal condensate construction are suppressed in volar skin.

Volar epithelium is the first on the body to differentiate into a keratinized, stratified epidermis, producing basal and intermediate K14+ve layers and a K10+ve suprabasal epidermis. We detect sporadic K14+ve suprabasal cells on all parts of human fetal skin but find these forming a continuous layer only on the volar skin during human development. This structure invariably precedes the emergence of fingerprint ridge downgrowths and extends proximally from the distal tip of the digit from week 12. Focal epithelial proliferation then drives the formation of downgrowths under a stiff suprabasal epidermis.[25] The properties of the softer K14+ve intermediate and basal layers are likely to be important for ridge formation, as heterozygous mutations in *KERATIN14* in Naegeli-Franceschetti-Jadassohn syndrome and dermatopathia pigmentosa reticularis (OMIM 161000, OMIM 125595) cause selective absence of fingerprints,[51] demonstrating a particular reliance of dermatoglyph formation on appropriate cytoskeletal structures in these layers. After termination of its downgrowth, ongoing cellular proliferation within the primary ridge produces a thick suprabasal epithelium that defines the corrugated surface ridges.

The size and shape of the volar pads on the fetal fingertip have long been recognized as a key determinant of fingerprint type, with large domed pads associated with whorls and small

Figure 6. Digit geometry determines fingerprint type through variable pattern initiation sites and boundaries

(A) H&E-stained sections of week 14 digit showing ridge initiation sites on the central volar pad of the distal phalanx (P3), at the nail bed, and at flexion creases.
(B and C) Expression of *EDAR* and LEF1 in 10 weeks digit volar pads (arrow).
(D) *RSPO2* expression in the volar pad mesenchyme (arrow) adjacent to the epithelium in a 10 weeks digit.
(E and F) Expression of *EDAR* and LEF1 in 13 weeks digits. Left, longitudinal sections; right, transverse sections. Arrows indicate areas of highest expression.
(G) *DKK1* expression (double-headed arrow) in 13 weeks digit.
(H) Projected confocal stack image of volar skin. Ridges close to a crease are aligned in parallel and ridges are suppressed within the crease.
(I) Skin flexion crease showing suppression of ridge formation and adjacent broad shallow ridges (arrows).
(J) *EDAR* and *FGF20* expression in creases.
(K) Quantification of epithelial proliferation in creases compared to ridges and interridges. Each point represents an individual sample.
(L) Quantification of ridge morphology and spacing relative to crease centers. Error bars represent SEM from analysis of 11 creases, each from an independent sample.
(M) Spreading waves of ridge formation produce a triradius at their confluence (arrows). Whole mounted skin from two different digits is shown.
(N) Toluidine blue-stained 16 weeks digit showing different patterning complexes (PC, bracketed). Cr., crease.
(O) Simulations of periodic patterning at fingertip with initiation sites at volar pad, dorsal-ventral boundary and distal digital crease. Varying the shape and location of each initiation readily produces arch, loop or whorl patterns.
(P) Schematic of molecular and cellular events producing digit ridges on the volar pad and hair follicles on other regions of the skin. Dotted lines indicate epithelial-mesenchymal junctions or outline phalanges. Ep., epithelium; Me., mesenchyme. Scale bars, 500 μm (A upper, B left, C left, D upper, E– H, and N); 250 μm (M); 50 μm (A lower, B right, C right, D lower, I, and J).
See also Figures S5 and S6.

or absent pads associated with arch formation.[7] A recent genomewide association study[9] reports that most of the genes influencing arch, loop, or whorl selection act prior to ridge emergence and so have an indirect effect on fingerprint pattern. One of these genes, *RSPO2*, we identify as selectively expressed in volar pad mesenchyme underlying the trigger sites for ridge patterning in overlying epithelium. R-Spondins enhance WNT signaling, providing a mechanism for volar pad area, mass, and shape to influence fingerprint pattern through induction of the WNT-responsive patterning genes that begin the process of ridge formation. Variation at the *EDAR* locus is also associated with fingerprint type,[9] likely by influencing the location and timing of *EDAR* expression to define the key pattern initiation sites of the volar pad apex and digit's dorsal-ventral boundary.

The early-forming flexion creases, placed by movement of the digits beginning at approximately week 12[52] and the shape of nearby volar pads,[42] suppress definitive ridge formation, and this zone of destabilized ridge identity serves as a boundary to organise ridge initiations nearby. The importance of these creases in organizing ridge orientation is underscored by the longitudinal rather than transverse ridges along the digits, and the extension of loop or whorl patterns proximally to the medial phalanx, when creases do not form due to impaired movement of the digit *in utero*.[53–55]

In mouse, the dermatoglyph ridges form on a small field, limiting the complexity of the pattern to a simple set of parallel stripes. However, on a sufficiently large domain, such as the week 12 human digit tip, the pattern forming system for laying out parallel ridges is configurable into arch, loop, or whorl patterns by interaction with anatomical landmarks. Our simulations of such a system can readily explain fingerprint arrangements simply by varying their initiation locations. Indeed, almost indistinguishable arch, loop, and whorl fingerprint types are found in both koala and human,[23] illustrating the ease of their generation by a patterning system that responds to the anatomical landmarks of the dorsal-ventral boundary, volar pad and flexion creases, of the distal digit. The uniqueness of fingerprints is accentuated by the noise-driven initiation and minute random differences characteristic of Turing patterns, added to by the later sweat gland patterning that leaves a row of periodic pores along the ridge apices, generating a richly detailed fine structure that permits individual identification.

Taken together, our findings show that dermatoglyph ridges are a developmentally abbreviated ectodermal appendage, with their proverbial diversity arising from deployment of a simple molecular patterning system responsive to a set of highly variable anatomical initiation sites.

Limitations of the study

Ridge inhibitory factors other than BMPs may act in the patterning process, which could explain why complete transformation of volar epithelium to ridge was not attained by suppressing BMP function. The small size of the mouse digit prevents the elaboration of complex patterns such as arches, loops, or whorls, and so studies in this species are limited to understanding mechanisms defining ridge-to-ridge periodicity. Functional experiments *in vivo* are clearly not possible in human, thus longer-term culture methods or organoids that specifically model volar skin formation must be developed to enable deeper study of ridge and sweat gland morphogenesis.

STAR★METHODS

Detailed methods are provided in the online version of this paper and include the following:

- KEY RESOURCES TABLE
- RESOURCE AVAILABILITY
  - Lead contact
  - Materials availability
  - Data and code availability
- EXPERIMENTAL MODEL AND SUBJECT DETAILS
  - Fetal specimens
  - Cell lines
  - Mice
- METHOD DETAILS
  - Toluidine blue staining
  - Sample preparation & histology
  - Immunofluorescence
  - *In situ* hybridization
  - Fibroblast culture and experiments
  - Single nucleus RNA sequencing and data processing
  - Identifying ridge and hair placode markers
  - Atomic force microscopy
  - Skin organoids
  - *Ex vivo* skin culture, treatment and qPCR
  - Wavelet analysis of pre-pattern
  - Mathematical simulations
- QUANTIFICATION AND STATISTICAL ANALYSIS
  - Primary ridge wavelength measurements
  - Structural analyses
  - Cell density and proliferation quantification
  - Ridge morphology and proliferation analysis
  - Mouse digit ridge analysis
  - Flexion crease measurements

SUPPLEMENTAL INFORMATION

Supplemental information can be found online at https://doi.org/10.1016/j.cell.2023.01.015.

ACKNOWLEDGMENTS

We thank the Centre for Regenerative Medicine Single-cell Multi-omics service and Flow Cytometry Facility, and the Genetics Core, Edinburgh Clinical Research Facility, for single nucleus library production and sequencing. This study was funded by BBSRC awards BB/N008545/1, BB/T007788/1, BBS/E/D/10002071, BB/T008385/1, and BB/CCG1780/1; Wellcome Trust Senior Research Fellowship award to S.J.B. (220875/Z/20/Z); NSFC (32200482); and ERDF-Project CZ.02.1.01/0.0/0.0/16-019/0000778. Y.C. and C.A. received funding from an EPSRC Doctoral Training Partnership Scholarship. This work was in part undertaken at the MRC Centre for Reproductive Health which is funded by the MRC Centre grant MR/N022556/1.

AUTHOR CONTRIBUTIONS

Conceptualization: J.D.G., Z.R.S., A.L.K., J.R., A.B., J.L., V.K., T.E.W., E.A.G., S.W., M.L.C., D.J.H.

Methodology and resources: J.D.G., Z.R.S., B.B.-J.S., L.C., A.L.K., C.A., V.K., T.E.W., E.A.G., R.A.A., L.J.J., S.J.B., Y.C., M.L.C., D.J.H.

Analysis and investigation: J.D.G., Z.R.S., B.B.-J.S., C.B.-S., L.C., C.A., J.R., A.C., L.J.J., Y.C., M.L.C., D.J.H.

Writing – Original Draft: J.D.G., Z.R.S., A.L.K., V.K., T.E.W., E.A.G., Y.C., M.L.C., D.J.H. All authors contributed to manuscript review and editing.

DECLARATION OF INTERESTS

The authors declare no competing interests.

Received: February 16, 2022
Revised: November 4, 2022
Accepted: January 10, 2023
Published: February 9, 2023

REFERENCES

1. Yum, S.M., Baek, I.K., Hong, D., Kim, J., Jung, K., Kim, S., Eom, K., Jang, J., Kim, S., Sattorov, M., et al. (2020). Fingerprint ridges allow primates to regulate grip. Proc. Natl. Acad. Sci. USA *117*, 31665–31673. https://doi.org/10.1073/pnas.2001055117.
2. Scheibert, J., Leurent, S., Prevost, A., and Debrégeas, G. (2009). The role of fingerprints in the coding of tactile information probed with a biomimetic sensor. Science *323*, 1503–1506. https://doi.org/10.1126/science.1166467.
3. Galton, F. (1892). Finger Prints (Macmillan and co.).
4. Verbov, J. (1970). Clinical significance and genetics of epidermal ridges–a review of dermatoglyphics. J. Invest. Dermatol. *54*, 261–271. https://doi.org/10.1111/1523-1747.ep12258550.
5. Miller, J.R. (1973). Dermatoglyphics. J. Invest. Dermatol. *60*, 435–442. https://doi.org/10.1111/1523-1747.ep12702906.
6. Saxena, N., Mok, K.W., and Rendl, M. (2019). An updated classification of hair follicle morphogenesis. Exp. Dermatol. *28*, 332–344. https://doi.org/10.1111/exd.13913.
7. Babler, W.J. (1991). Embryologic development of epidermal ridges and their configurations. Birth Defects Orig. Artic. Ser. *27*, 95–112.
8. Wertheim, K., and Maceo, A. (2002). The critical stage of friction ridge and pattern formation. J. Forensic Ident. *52*, 35–85.
9. Li, J., Glover, J.D., Zhang, H., Peng, M., Tan, J., Mallick, C.B., Hou, D., Yang, Y., Wu, S., Liu, Y., et al. (2022). Limb development genes underlie variation in human fingerprint patterns. Cell *185*, 95–112.e18. https://doi.org/10.1016/j.cell.2021.12.008.
10. Lacroix, B., Wolff-Quenot, M.J., and Haffen, K. (1984). Early human hand morphology: an estimation of fetal age. Early Hum. Dev. *9*, 127–136. https://doi.org/10.1016/0378-3782(84)90093-8.
11. Kücken, M. (2007). Models for fingerprint pattern formation. Forensic Sci. Int. *171*, 85–96. https://doi.org/10.1016/j.forsciint.2007.02.025.
12. Düring, B., Gottschlich, C., Huckemann, S., Kreusser, L.M., and Schönlieb, C.B. (2019). An anisotropic interaction model for simulating fingerprints. J. Math. Biol. *78*, 2171–2206. https://doi.org/10.1007/s00285-019-01338-3.
13. Gupta, K., Levinsohn, J., Linderman, G., Chen, D., Sun, T.Y., Dong, D., Taketo, M.M., Bosenberg, M., Kluger, Y., Choate, K., and Myung, P. (2019). Single-cell analysis reveals a hair follicle dermal niche molecular differentiation trajectory that begins prior to morphogenesis. Dev. Cell *48*, 17–31.e6. https://doi.org/10.1016/j.devcel.2018.11.032.
14. Tsai, S.Y., Sennett, R., Rezza, A., Clavel, C., Grisanti, L., Zemla, R., Najam, S., and Rendl, M. (2014). Wnt/beta-catenin signaling in dermal condensates is required for hair follicle formation. Dev. Biol. *385*, 179–188. https://doi.org/10.1016/j.ydbio.2013.11.023.
15. Glover, J.D., Wells, K.L., Matthäus, F., Painter, K.J., Ho, W., Riddell, J., Johansson, J.A., Ford, M.J., Jahoda, C.A.B., Klika, V., et al. (2017). Hierarchical patterning modes orchestrate hair follicle morphogenesis. PLoS Biol. *15*, e2002117. https://doi.org/10.1371/journal.pbio.2002117.
16. Huh, S.H., Närhi, K., Lindfors, P.H., Häärä, O., Yang, L., Ornitz, D.M., and Mikkola, M.L. (2013). Fgf20 governs formation of primary and secondary dermal condensations in developing hair follicles. Genes Dev. *27*, 450–458. https://doi.org/10.1101/gad.198945.112.
17. Nousbeck, J., Burger, B., Fuchs-Telem, D., Pavlovsky, M., Fenig, S., Sarig, O., Itin, P., and Sprecher, E. (2011). A mutation in a skin-specific isoform of SMARCAD1 causes autosomal-dominant adermatoglyphia. Am. J. Hum. Genet. *89*, 302–307. https://doi.org/10.1016/j.ajhg.2011.07.004.
18. Song, Y., Boncompagni, A.C., Kim, S.S., Gochnauer, H.R., Zhang, Y., Loots, G.G., Wu, D., Li, Y., Xu, M., and Millar, S.E. (2018). Regional control of hairless versus hair-bearing skin by Dkk2. Cell Rep. *25*, 2981–2991.e3. https://doi.org/10.1016/j.celrep.2018.11.017.
19. Qu, R., Gupta, K., Dong, D., Jiang, Y., Landa, B., Saez, C., Strickland, G., Levinsohn, J., Weng, P.L., Taketo, M.M., et al. (2022). Decomposing a deterministic path to mesenchymal niche formation by two intersecting morphogen gradients. Dev. Cell *57*, 1053–1067.e5. https://doi.org/10.1016/j.devcel.2022.03.011.
20. Singh, B., and Coffey, R.J. (2014). From wavy hair to naked proteins: the role of transforming growth factor alpha in health and disease. Semin. Cell Dev. Biol. *28*, 12–21. https://doi.org/10.1016/j.semcdb.2014.03.003.
21. Shirokova, V., Biggs, L.C., Jussila, M., Ohyama, T., Groves, A.K., and Mikkola, M.L. (2016). Foxi3 deficiency compromises hair follicle stem cell specification and activation. Stem Cell. *34*, 1896–1908. https://doi.org/10.1002/stem.2363.
22. Hillman, R.T., Feng, B.Y., Ni, J., Woo, W.M., Milenkovic, L., Hayden Gephart, M.G., Teruel, M.N., Oro, A.E., Chen, J.K., and Scott, M.P. (2011). Neuropilins are positive regulators of Hedgehog signal transduction. Genes Dev. *25*, 2333–2346. https://doi.org/10.1101/gad.173054.111.
23. Kücken, M., and Newell, A.C. (2005). Fingerprint formation. J. Theor. Biol. *235*, 71–83. https://doi.org/10.1016/j.jtbi.2004.12.020.
24. Totaro, A., Panciera, T., and Piccolo, S. (2018). YAP/TAZ upstream signals and downstream responses. Nat. Cell Biol. *20*, 888–899. https://doi.org/10.1038/s41556-018-0142-z.
25. Fiore, V.F., Krajnc, M., Quiroz, F.G., Levorse, J., Pasolli, H.A., Shvartsman, S.Y., and Fuchs, E. (2020). Mechanics of a multilayer epithelium instruct tumour architecture and function. Nature *585*, 433–439. https://doi.org/10.1038/s41586-020-2695-9.
26. Li, S., Zhou, J., Bu, J., Ning, K., Zhang, L., Li, J., Guo, Y., He, X., He, H., Cai, X., et al. (2017). Ectodysplasin A protein promotes corneal epithelial cell proliferation. J. Biol. Chem. *292*, 13391–13401. https://doi.org/10.1074/jbc.M117.803809.
27. Schmidt-Ullrich, R., Tobin, D.J., Lenhard, D., Schneider, P., Paus, R., and Scheidereit, C. (2006). NF-kappaB transmits Eda A1/EdaR signalling to activate Shh and cyclin D1 expression, and controls post-initiation hair placode down growth. Development *133*, 1045–1057. https://doi.org/10.1242/dev.02278.
28. Williams, R., Jobling, S., Sims, A.H., Mou, C., Wilkinson, L., Collu, G.M., Streuli, C.H., Gilmore, A.P., Headon, D.J., and Brennan, K. (2022). Elevated EDAR signalling promotes mammary gland tumourigenesis with squamous metaplasia. Oncogene *41*, 1040–1049. https://doi.org/10.1038/s41388-021-01902-6.
29. Headon, D.J., and Overbeek, P.A. (1999). Involvement of a novel Tnf receptor homologue in hair follicle induction. Nat. Genet. *22*, 370–374. https://doi.org/10.1038/11943.
30. Zhang, Y., Tomann, P., Andl, T., Gallant, N.M., Huelsken, J., Jerchow, B., Birchmeier, W., Paus, R., Piccolo, S., Mikkola, M.L., et al. (2009). Reciprocal requirements for EDA/EDAR/NF-kappaB and Wnt/beta-catenin signaling pathways in hair follicle induction. Dev. Cell *17*, 49–61. S1534-5807(09)00213-5 [pii]. https://doi.org/10.1016/j.devcel.2009.05.011.
31. Mou, C., Jackson, B., Schneider, P., Overbeek, P.A., and Headon, D.J. (2006). Generation of the primary hair follicle pattern. Proc. Natl. Acad.

Sci. USA *103*, 9075–9080. 0600825103 [pii]. https://doi.org/10.1073/pnas.0600825103.

32. Pummila, M., Fliniaux, I., Jaatinen, R., James, M.J., Laurikkala, J., Schneider, P., Thesleff, I., and Mikkola, M.L. (2007). Ectodysplasin has a dual role in ectodermal organogenesis: inhibition of Bmp activity and induction of Shh expression. Development *134*, 117–125. https://doi.org/10.1242/dev.02708.
33. Verbov, J. (1970). Hypohidrotic (or anhidrotic) ectodermal dysplasia–an appraisal of diagnostic methods. Br. J. Dermatol. *83*, 341–348.
34. Kargül, B., Alcan, T., Kabalay, U., and Atasu, M. (2001). Hypohidrotic ectodermal dysplasia: dental, clinical, genetic and dermatoglyphic findings of three cases. J. Clin. Pediatr. Dent *26*, 5–12.
35. Mou, C., Thomason, H.A., Willan, P.M., Clowes, C., Harris, W.E., Drew, C.F., Dixon, J., Dixon, M.J., and Headon, D.J. (2008). Enhanced ectodysplasin-A receptor (EDAR) signaling alters multiple fiber characteristics to produce the East Asian hair form. Hum. Mutat. *29*, 1405–1411. https://doi.org/10.1002/humu.20795.
36. Painter, K.J., Hunt, G.S., Wells, K.L., Johansson, J.A., and Headon, D.J. (2012). Towards an integrated experimental-theoretical approach for assessing the mechanistic basis of hair and feather morphogenesis. Interface Focus *2*, 433–450. https://doi.org/10.1098/rsfs.2011.0122.
37. Sheth, R., Marcon, L., Bastida, M.F., Junco, M., Quintana, L., Dahn, R., Kmita, M., Sharpe, J., and Ros, M.A. (2012). Hox genes regulate digit patterning by controlling the wavelength of a Turing-type mechanism. Science *338*, 1476–1480. https://doi.org/10.1126/science.1226804.
38. Lee, J., Rabbani, C.C., Gao, H., Steinhart, M.R., Woodruff, B.M., Pflum, Z.E., Kim, A., Heller, S., Liu, Y., Shipchandler, T.Z., and Koehler, K.R. (2020). Hair-bearing human skin generated entirely from pluripotent stem cells. Nature *582*, 399–404. https://doi.org/10.1038/s41586-020-2352-3.
39. Botchkarev, V.A., Botchkareva, N.V., Roth, W., Nakamura, M., Chen, L.H., Herzog, W., Lindner, G., McMahon, J.A., Peters, C., Lauster, R., et al. (1999). Noggin is a mesenchymally derived stimulator of hair-follicle induction. Nat. Cell Biol. *1*, 158–164. https://doi.org/10.1038/11078.
40. Jamora, C., DasGupta, R., Kocieniewski, P., and Fuchs, E. (2003). Links between signal transduction, transcription and adhesion in epithelial bud development. Nature *422*, 317–322. https://doi.org/10.1038/nature01458.
41. Kratochwil, K., Dull, M., Farinas, I., Galceran, J., and Grosschedl, R. (1996). Lef1 expression is activated by BMP-4 and regulates inductive tissue interactions in tooth and hair development. Genes Dev. *10*, 1382–1394. https://doi.org/10.1101/gad.10.11.1382.
42. Kimura, S., Schaumann, B.A., Plato, C.C., and Kitagawa, T. (1990). Embryological development and prevalence of digital flexion creases. Anat. Rec. *226*, 249–257. https://doi.org/10.1002/ar.1092260214.
43. David, T.J. (1973). Congenital malformations of human dermatoglyphs. Arch. Dis. Child. *48*, 191–198. https://doi.org/10.1136/adc.48.3.191.
44. Biggs, L.C., and Mikkola, M.L. (2014). Early inductive events in ectodermal appendage morphogenesis. Semin. Cell Dev. Biol. *25–26*, 11–21. https://doi.org/10.1016/j.semcdb.2014.01.007.
45. Kondo, S., and Miura, T. (2010). Reaction-diffusion model as a framework for understanding biological pattern formation. Science *329*, 1616–1620. https://doi.org/10.1126/science.1179047.
46. Vanag, V.K., and Epstein, I.R. (2009). Pattern formation mechanisms in reaction-diffusion systems. Int. J. Dev. Biol. *53*, 673–681. https://doi.org/10.1387/ijdb.072484vv.
47. Richardson, G.D., Bazzi, H., Fantauzzo, K.A., Waters, J.M., Crawford, H., Hynd, P., Christiano, A.M., and Jahoda, C.A.B. (2009). KGF and EGF signalling block hair follicle induction and promote interfollicular epidermal fate in developing mouse skin. Development *136*, 2153–2164. https://doi.org/10.1242/dev.031427.
48. Schneider, H., Faschingbauer, F., Schuepbach-Mallepell, S., Körber, I., Wohlfart, S., Dick, A., Wahlbuhl, M., Kowalczyk-Quintas, C., Vigolo, M., Kirby, N., et al. (2018). Prenatal correction of X-linked hypohidrotic ectodermal dysplasia. N. Engl. J. Med. *378*, 1604–1610. https://doi.org/10.1056/NEJMoa1714322.
49. Lu, C.P., Polak, L., Keyes, B.E., and Fuchs, E. (2016). Spatiotemporal antagonism in mesenchymal-epithelial signaling in sweat versus hair fate decision. Science *354*, aah6102. https://doi.org/10.1126/science.aah6102.
50. Kamberov, Y.G., Karlsson, E.K., Kamberova, G.L., Lieberman, D.E., Sabeti, P.C., Morgan, B.A., and Tabin, C.J. (2015). A genetic basis of variation in eccrine sweat gland and hair follicle density. Proc. Natl. Acad. Sci. USA *112*, 9932–9937. https://doi.org/10.1073/pnas.1511680112.
51. Lugassy, J., Itin, P., Ishida-Yamamoto, A., Holland, K., Huson, S., Geiger, D., Hennies, H.C., Indelman, M., Bercovich, D., Uitto, J., et al. (2006). Naegeli-Franceschetti-Jadassohn syndrome and dermatopathia pigmentosa reticularis: two allelic ectodermal dysplasias caused by dominant mutations in KRT14. Am. J. Hum. Genet. *79*, 724–730. https://doi.org/10.1086/507792.
52. Pooh, R., and Ogura, T. (2004). Normal and abnormal fetal hand positioning and movement in early pregnancy detected by three- and four-dimensional ultrasound. Ultrasound Rev. Obstet. Gynecol. *4*, 46–51. https://doi.org/10.3109/14722240410001700249.
53. Fried, K., and Mundel, G. (1976). Absence of distal interphalangeal creases of fingers with flexion limitation. J. Med. Genet. *13*, 127–130. https://doi.org/10.1136/jmg.13.2.127.
54. Casey, P.A., and Ger, E. (1979). Abnormal dermatoglyphics in arthrogryposis multiplex congenita. Hand *11*, 34–40. https://doi.org/10.1016/s0072-968x(79)80006-6.
55. Sack, G.H., Jr. (1978). A dominantly inherited form of arthrogryposis multiplex congenita with unusual dermatoglyphics. Clin. Genet. *14*, 317–323. https://doi.org/10.1111/j.1399-0004.1978.tb02096.x.
56. Ferrer-Vaquer, A., Piliszek, A., Tian, G., Aho, R.J., Dufort, D., and Hadjantonakis, A.K. (2010). A sensitive and bright single-cell resolution live imaging reporter of Wnt/ss-catenin signaling in the mouse. BMC Dev. Biol. *10*, 121. https://doi.org/10.1186/1471-213X-10-121.
57. Schindelin, J., Arganda-Carreras, I., Frise, E., Kaynig, V., Longair, M., Pietzsch, T., Preibisch, S., Rueden, C., Saalfeld, S., Schmid, B., et al. (2012). Fiji: an open-source platform for biological-image analysis. Nat. Methods *9*, 676–682. https://doi.org/10.1038/nmeth.2019.
58. Aigouy, B., Umetsu, D., and Eaton, S. (2016). Segmentation and quantitative analysis of epithelial tissues. Methods Mol. Biol. *1478*, 227–239. https://doi.org/10.1007/978-1-4939-6371-3_13.
59. Stuart, T., Butler, A., Hoffman, P., Hafemeister, C., Papalexi, E., Mauck, W.M., 3rd, Hao, Y., Stoeckius, M., Smibert, P., and Satija, R. (2019). Comprehensive integration of single-cell data. Cell *177*, 1888–1902.e21. https://doi.org/10.1016/j.cell.2019.05.031.
60. Hao, Y., Hao, S., Andersen-Nissen, E., Mauck, W.M., 3rd, Zheng, S., Butler, A., Lee, M.J., Wilk, A.J., Darby, C., Zager, M., et al. (2021). Integrated analysis of multimodal single-cell data. Cell *184*, 3573–3587.e29. https://doi.org/10.1016/j.cell.2021.04.048.
61. Amezquita, R.A., Lun, A.T.L., Becht, E., Carey, V.J., Carpp, L.N., Geistlinger, L., Marini, F., Rue-Albrecht, K., Risso, D., Soneson, C., et al. (2020). Orchestrating single-cell analysis with Bioconductor. Nat. Methods *17*, 137–145. https://doi.org/10.1038/s41592-019-0654-x.
62. McCarthy, D.J., Campbell, K.R., Lun, A.T.L., and Wills, Q.F. (2017). Scater: pre-processing, quality control, normalization and visualization of single-cell RNA-seq data in R. Bioinformatics *33*, 1179–1186. https://doi.org/10.1093/bioinformatics/btw777.
63. Germain, P.L., Lun, A., Garcia Meixide, C., Macnair, W., and Robinson, M.D. (2021). Doublet identification in single-cell sequencing data using scDblFinder. F1000Res. *10*, 979. https://doi.org/10.12688/f1000research.73600.1.
64. Yang, S., Corbett, S.E., Koga, Y., Wang, Z., Johnson, W.E., Yajima, M., and Campbell, J.D. (2020). Decontamination of ambient RNA in single-cell

RNA-seq with DecontX. Genome Biol. *21*, 57. https://doi.org/10.1186/s13059-020-1950-6.

65. Moon, K.R., van Dijk, D., Wang, Z., Gigante, S., Burkhardt, D.B., Chen, W.S., Yim, K., Elzen, A.V.D., Hirn, M.J., Coifman, R.R., et al. (2019). Visualizing structure and transitions in high-dimensional biological data. Nat. Biotechnol. *37*, 1482–1492. https://doi.org/10.1038/s41587-019-0336-3.
66. Street, K., Risso, D., Fletcher, R.B., Das, D., Ngai, J., Yosef, N., Purdom, E., and Dudoit, S. (2018). Slingshot: cell lineage and pseudotime inference for single-cell transcriptomics. BMC Genom. *19*, 477. https://doi.org/10.1186/s12864-018-4772-0.
67. Olhede, S.C., and Walden, A.T. (2002). Generalized morse wavelets. IEEE Trans. Signal Process. *50*, 2661–2670.
68. Misiti, M., Misiti, Y., Oppenheim, G., and Poggi, J.M. (1996). Wavelet Toolbox User's Guide (The MathWorks).
69. Kolokolnikov, T., Sun, W., Ward, M., and Wei, J. (2006). The stability of a stripe for the gierer–meinhardt model and the effect of saturation. SIAM J. Appl. Dyn. Syst. *5*, 313–363.
70. Van Gorder, R.A., Klika, V., and Krause, A.L. (2021). Turing conditions for pattern forming systems on evolving manifolds. J. Math. Biol. *82*, 4. https://doi.org/10.1007/s00285-021-01552-y.
71. Domander, R., Felder, A.A., and Doube, M. (2021). BoneJ2 - refactoring established research software. Wellcome Open Res. *6*, 37. https://doi.org/10.12688/wellcomeopenres.16619.2.

STAR★METHODS

KEY RESOURCES TABLE

REAGENT or RESOURCE	SOURCE	IDENTIFIER
Antibodies		
Mouse anti-cytokeratin 14 antibody [LL002], (1:1000, Citrate)	Abcam	Cat# ab7800; RRID:AB_306091
Rabbit recombinant anti-Ki67 antibody [SP6], (1:200, Citrate)	Abcam	Cat# ab16667; RRID:AB_302549
Rabbit anti-cytokeratin 10 antibody [RKSE60], (1:600, Citrate)	Abcam	Cat# ab9025; RRID:AB_2134556
Rabbit recombinant anti-beta catenin antibody [E247], (1:500, Citrate)	Abcam	Cat# ab32572; RRID:AB_725966
Mouse anti-α E-catenin antibody (G-11), (1:100, Citrate)	Santa Cruz	Cat# sc-9988; RRID:AB_626805
Rabbit recombinant anti-LEF1 antibody [EPR2029Y], (1:200, Citrate)	Abcam	Cat# ab137872; RRID:AB_2892647
Rabbit anti-laminin antibody (1:200, Proteinase K)	Abcam	Cat# ab11575; RRID:AB_298179
Rabbit recombinant anti-phospho-SMAD1/SMAD5 (Ser463, Ser465) antibody (31H14L11), (1:200, Citrate)	Thermo Fisher	Cat# 700047; RRID:AB_2532276
Rabbit anti-SOX2 antibody, (1:500, Citrate)	Abcam	Cat# ab97959; RRID:AB_2341193
Mouse anti-YAP1 antibody (63.7), (1:100, Citrate)	Santa Cruz	Cat# sc-101199; RRID:AB_1131430
Rabbit recombinant anti-active YAP1 antibody [EPR19812], (1:200, Citrate)	Abcam	Cat# ab205270; RRID:AB_2813833
Rabbit recombinant anti-integrin alpha 6 antibody [EPR18124], (1:200, Citrate)	Abcam	Cat# ab181551; RRID:AB_2927695
Rabbit anti-SMARCAD1 antibody, (1:200, Citrate)	Atlas	Cat# HPA016737; RRID:AB_1857271
Chicken anti-GFP antibody, (1:250, Citrate)	Abcam	Cat# ab13970; RRID:AB_300798
Rabbit anti-ARL13B antibody, (1:500, Citrate)	Proteintech	Cat# 17711-1AP; RRID:AB_2060867
Mouse anti-acetylated tubulin antibody, (1:500, Citrate)	Sigma-Aldrich	Cat# T7451; RRID:AB_609894
Rabbit anti-phospho-EGF receptor (Tyr1068) (D7A5) XP, (1:100, Citrate)	Cell Signaling Technologies	Cat# 3777S; RRID:AB_2096270
Rabbit anti-cytokeratin 8 antibody, (1:200, Citrate)	Abcam	Cat# ab59400; RRID:AB_942041
Goat anti-Rabbit IgG (H + L) Highly Cross-Adsorbed Secondary Antibody, Alexa Fluor 546, (1:500)	Thermo Fisher	Cat# A11035; RRID:AB_2534093
Goat anti-Rabbit IgG (H + L) Highly Cross-Adsorbed Secondary Antibody, Alexa Fluor 647. (1:500)	Thermo Fisher	Cat# A21245; RRID:AB_2535813
Goat anti-Mouse IgG (H + L) Highly Cross-Adsorbed Secondary Antibody, Alexa Fluor 488, (1:500)	Thermo Fisher	Cat# A11029; RRID:AB_2534088
Alexa Fluor 647 Phalloidin, (1:200)	Thermo Fisher	Cat# A22287; RRID:AB_2620155
Biological samples		
Human fetal samples	Royal Infirmary of Edinburgh	N/A

(*Continued on next page*)

Continued

REAGENT or RESOURCE	SOURCE	IDENTIFIER
Chemicals, peptides, and recombinant proteins		
4′,6-Diamidino-2-phenylindole dihydrochloride (DAPI), (1:5000)	Sigma-Aldrich	Cat# D9542
Opal Dye 520, (1:1500)	Akoya biosciences	Cat# OP-001001
Opal Dye 570, (1:1500)	Akoya biosciences	Cat# OP-001003
Opal Dye 620, (1:1500)	Akoya biosciences	Cat# OP-001004
Opal Dye 690, (1:1500)	Akoya biosciences	Cat# OP-001006
Recombinant Human R-Spondin 2 protein	R & D Systems	Cat# 3266-RS
Recombinant Human Wnt-3a	R & D Systems	Cat# 5036-WN
Recombinant Human FGF-20	R & D Systems	Cat# 2547-FG
Recombinant Human/Mouse/Rat BMP2	R & D Systems	Cat# 355-BM
Recombinant Human FGF-basic	Peprotech	Cat# 100-18B
Recombinant Human BMP-4	Peprotech	Cat# 120–05
CHIR99021	Stem Cell Technologies	Cat# 72052
LDN193189	Sigma-Aldrich	Cat# SML0559
LDN193189	Stemgent	Cat# A8324
LGK-974	Selleckchem	Cat# S7143
FH535	Sigma-Aldrich	Cat# F5682
Y27632	Stemgent	Cat# AMS.04-0012-02
SB431542	Stemgent	Cat# AMS.04-0010-05
Vitronectin	Gibco	Cat# 15134499
Accutase	Gibco	Cat# A11105-01
Normocin	Invivogen	Cat# ant-nr-05
Matrigel	Corning	Cat# 356230
Glutamax	Gibco	Cat# 35050–061
Versene	Gibco	Cat# 15040066
Trypsin (2.5%)	Gibco	Cat# 15090046
Collagenase D	Roche	Cat# 11088858001
B-27 Supplement	Gibco	Cat# 12587–010
N2 Supplement	Gibco	Cat# 17502–048
2-Mercaptoethanol	Gibco	Cat# 21985023
E8 Medium	Gibco	Cat# A2858501
E6 Medium	Gibco	Cat# A1516401
DMEM/F12 medium	Gibco	Cat# 12634–010
Neurobasal Medium	Gibco	Cat# 21103–049
Dulbecco's Modified Eagle's Medium	Sigma-Aldrich	Cat# D5796
BSA	Tocris Bioscience	Cat# 5217
Fetal Bovine Serum	Gibco	Cat# 10270106
Goat Serum	Sigma-Aldrich	Cat# G9023
Gelatin	Sigma-Aldrich	Cat# G2500
Sucrose	Sigma-Aldrich	Cat# S0389
Methyl Cellulose	Sigma-Aldrich	Cat# M7027
Superscript III First- Strand Synthesis Kit	Thermo Fisher	Cat# 4913850001
Tri-Reagent	Sigma-Aldrich	Cat# 93289
Random Primers	Promega	Cat# C1181
FastStart Universal Sybr Green Master (Rox)	Sigma-Aldrich	Cat# 4913850001
RNAsin Plus	Promega	Cat# N2615
Nuclei EZ Lysis Buffer	Sigma-Aldrich	Cat# N3408

(*Continued on next page*)

Continued

REAGENT or RESOURCE	SOURCE	IDENTIFIER
5-Bromo-4-chloro-3-indolyl phosphate p-toluidine salt	Sigma-Aldrich	Cat# B8503
TrueBlack	Biotium	Cat# 23007
ProLong Gold Antifade Mountant	Thermo Fisher	Cat# P36930
Tween 20	Fisher Chemical	Cat# BP337
Tween 80	Sigma-Aldrich	Cat# P5188
Triton X-100	Sigma-Aldrich	Cat# X100
cOmplete Protease Inhibitor Cocktail	Sigma-Aldrich	Cat# 11697498001
Proteinase K	Thermo Fisher	Cat# EO0491
Potassium Hydroxide	Sigma-Aldrich	Cat# 221473
10% Neutral Buffered Formalin	Sigma-Aldrich	Cat# HT501128
Dimethyl Sulfoxide	Sigma-Adrich	Cat# D2650
Critical commercial assays		
Click-iT EdU Cell Proliferation Kit for Imaging, Alexa Fluor 555 dye	Thermo Fisher	Cat# C10338
RNAscope Multiplex Fluorescent Reagent Kit v2	ACD Bioscience	Cat# 323100
Chromium Next GEM Single Cell 3′ GEM, Library & Gel Bead Kit v3.1	10x Genomics	Cat# 1000121
NextSeq 1000/2000 P3 Reagents (100 cycles) v3 Kit	Illumina	Cat# 20040559
PhiX Control v3	Illumina	Cat# FC-110-3001
Deposited data		
snRNA-seq data	This paper	GEO: GSE195657
Experimental models: Cell lines		
Mono-allelic mEGFP Tagged DSP WTC iPSC Line	Coriell Institute	Cat# AICS-0017
Experimental models: Organisms/strains		
Mouse: TCF/Lef::H2B-GFP	Ferrer-Vaquer et al.[56]	N/A
Mouse: Tabby (Eda^{Ta})	Roslin Institute	N/A
Mouse: $Edar^{Tg951}$	Roslin Institute	N/A
Mouse: $Egfr^{Wa5}$	Roslin Institute	N/A
Oligonucleotides		
See Table S2		N/A
Software and algorithms		
Zen	Carl Zeiss	RRID:SCR_013672
Adobe Photoshop	Adobe	RRID:SCR_014199
Fiji	Schindelin et al.,[57] SciJava	RRID:SCR_002285
Tissue Analyzer	Aigouy et al.[58]	https://github.com/baigouy/tissue_analyzer
MxPro	Stratagene	RRID:SCR_016375
Prism 9	GraphPad	RRID:SCR_002798
MATLAB	MathWorks	RRID:SCR_001622
COMSOL Multiphysics	COMSOL	RRID:SCR_014767
R		RRID:SCR_001905
Seurat		RRID:SCR_016341
scater		RRID:SCR_015954

(*Continued on next page*)

Continued

REAGENT or RESOURCE	SOURCE	IDENTIFIER
BioRender	BioRender	www.biorender.com
JPK data analysis software	Bruker	www.bruker.com
Mathematical simulation code	This paper	https://github.com/AndrewLKrause/fingerprint-simulations

RESOURCE AVAILABILITY

Lead contact

Further information and requests for resources should be directed to and will be fulfilled by the lead contact, Denis Headon (denis.headon@roslin.ed.ac.uk).

Materials availability

This study did not generate new unique reagents.

Data and code availability

- Single nucleus RNA-sequencing data have been deposited and are publicly available on NCBI Gene Expression Omnibus (GEO) as of the date of publication. The accession number is listed in the key resources table.
- Original code used for mathematical simulations has been deposited and is publicly available as of the date of publication at the GitHub repository, as in the key resources table.
- Any additional information required to reanalyze the data reported in this paper is available from the lead contact upon request.

EXPERIMENTAL MODEL AND SUBJECT DETAILS

Fetal specimens

Fetal tissue samples were obtained after elective medical termination of pregnancy from the Royal Infirmary of Edinburgh, UK with informed consent (approved by the Lothian Research Ethics Committee, ref. 08/S1101/1). Only morphologically normal samples were included and samples from both sexes were used. Gestational age was estimated by ultrasound scan before the procedure and confirmed by measuring foot length afterward, and was noted as weeks + days EGA. Back skin was from between the shoulder blade and the lower ribs.

Cell lines

Human embryonic fibroblasts (HEFs) were derived from 12 weeks EGA volar, back and scalp skin samples. Fetal skin samples were washed in PBS and incubated in 0.5% trypsin (Gibco) with 0.24 mM Versene (Gibco) at 37°C for 1 h. Skin containing dermal fibroblasts was cultured with 0.5 mg/mL collagenase D (Roche) in DMEM/10% FBS overnight. Cultures were vortexed to dissociate the fibroblasts, filtered through a 100 μm strainer, and cultured in fresh DMEM/10% FBS.

The desmoplakin-mEGFP human iPSC line (Allen Institute for Cell Science, Coriell Institute) was used to produce skin organoids.

Mice

Animal experiments were approved by the Roslin Institute Animal Welfare and Ethical Review Board and carried out under UK Home Office license (P682B81E4). TCF/Lef::H2B-GFP,[56] *Eda*^{Ta} and *Edar*^{Tg951} mice were maintained on the FVB background. *Egfr*^{Wa5} mice carry the EGFRp.Asp833Gly encoding mutation and were derived from a C57BL/6J x CBA/J F1 cross. For timed matings noon on the day of detection of a copulatory plug was assigned E0.5. Intragastric gavage of pregnant mice was performed twice daily for the period of the experiment. Pharmacological agents were dissolved in 0.5% methylcellulose (Sigma-Aldrich), 0.5% Tween-80 (Sigma-Aldrich) in water. Vehicle control was DMSO (Sigma-Aldrich) in this solution. PORCN inhibitor LGK-974 (Selleckchem) was used at 8 mg/kg/dose and BMP signaling inhibitor LDN193189 (Sigma-Aldrich) at 20 mg/kg/dose. All mice were used for analyses without regard to sex.

METHOD DETAILS

Toluidine blue staining

Formalin fixed forelimbs from eight week old mice or donated fetal specimens were incubated in 5% KOH with gentle agitation for 48 h, vortexed and remaining epidermis removed with forceps. Samples were washed with H_2O, refixed in 10% neutral buffered formalin (NBF), washed in H_2O, stained using 0.05% Toluidine Blue for 30 s and photographed on an Olympus SZX10 stereo microscope.

Sample preparation & histology

Samples for staining were fixed in 10% NBF for 24 h at room temperature before processing into paraffin wax, cryoblocks (7.5% Gelatin, 15% Sucrose) at −80°C or transfer to 70% ethanol for storage at 4°C. For histological analyses slides were dewaxed and stained with haematoxylin and eosin (H&E) using a Leica Autostainer XL and imaged on a Nikon Ni brightfield microscope and a Hamamatsu Nanozoomer XR slide scanner.

Immunofluorescence

For immunohistochemistry on paraffin embedded tissues, 6 μm sections were dewaxed and underwent antigen retrieval using an Antigen Retriever 2100 (Aptum Biologics) and/or Proteinase K (Thermo Fisher) incubation (see key resources table for specific antibody retrieval conditions). Following antigen retrieval, sections were incubated in TBS, 0.1% Triton X-100 for 10 min, washed with TBS, 0.1% Tween 20 (TBST), incubated in blocking buffer (5% heat treated goat serum/TBST) for 1 h, then incubated overnight at 4°C with primary antibody diluted in blocking buffer (see key resources table for antibody details and dilutions). Following TBST washes sections were incubated for 1 h at RT with blocking buffer containing secondary antibodies (see key resources table). Samples were washed in TBST, then TBS and stained with TrueBlack (Biotium). Samples were counterstained with DAPI and mounted in Prolong Gold.

For immunofluorescence on cryoembedded samples the same protocol was followed without antigen retrieval and some modifications before the initial blocking step. Briefly, 10 μm sections were warmed for 30 min at room temperature then incubated at 37°C in PBS for a further 30 min to remove gelatin before incubation in TBS with 0.1% Triton X-100.

For EdU staining the Click-iT EdU Cell Proliferation Kit for Imaging, Alexa Fluor 555 dye (Thermo Fisher) was used according to manufacturer's instructions. Following incubation with the EdU cocktail, sections were washed with PBS/3% BSA before undergoing immunofluorescence performed as above from the blocking step.

For whole mount immunofluorescence freshly fixed tissue samples were washed in PBS containing 0.5% Triton X-100 (PBTx), incubated in blocking buffer (10% goat serum/PBTx) for 2 h at RT, then incubated in blocking buffer containing primary antibody (see key resources table) for 24 h at 4°C. Samples were washed in PBTx, incubated with blocking buffer containing secondary antibody and phalloidin (Thermo Fisher) for 24 h at 4°C, washed in PBTx, incubated with DAPI/PBTx for 1 h and mounted using Prolong Gold. Samples were imaged using a Zeiss LSM 880 confocal microscope.

In situ hybridization

RNA *in situ* hybridization was done using the RNAscope Fluorescent Multiplex V2 Assay (ACD Biosciences) following the manufacturer's protocol. Hybridization was done on 6 μm formalin fixed paraffin sections and detected using Opal Dyes (Akoya Biosciences). After *in situ* hybridization, samples were washed in TBST and immunofluorescence performed as above, from the blocking step and excluding TrueBlack staining. Samples were counterstained with DAPI, mounted in Prolong Gold and imaged using a Zeiss LSM 880 confocal microscope.

Fibroblast culture and experiments

For scratch assays, HEFs were seeded in 24 well tissue culture plates and grown to confluence. Cells were starved in serum free medium for 4 h and a wound was made in the fibroblast layer using a pipette tip. Serum free medium was replaced with DMEM containing 1% FBS and supplemented with recombinant human FGF20 (200 ng/mL, R & D Systems), CHIR99021 (5 μM, Stem Cell Technologies), FH535 (10 μM, Sigma-Aldrich) or vehicle controls (0.1% BSA/PBS, DMSO), and cultured for 24 h at 37°C, 5% CO_2. For live cell imaging experiments a Zeiss Live Cell Observer fitted with an incubation chamber was used. Wound closure was analyzed across the first 16 h of culture.

For hanging drop experiments, HEFs were harvested and resuspended at density of 2,500 cells per μL in standard fibroblast culture medium supplemented with recombinant human FGF20 (200 ng/mL, R&D Systems), CHIR99021 (5 μM, Stem Cell Technologies), FH535 (10 μM, Sigma-Aldrich) or vehicle controls (0.1% BSA/PBS, DMSO). For each experimental condition, at least ten individual 10 μL drops were pipetted onto the lid of a 100 mm culture dish. The dish was filled with 5 mls of PBS and the lid inverted and placed on the dish. Hanging drop cultures were incubated at 37°C, 5% CO_2 for 48 h and imaged using a Zeiss Axiozoom V16 inverted microscope. Ten individual aggregates were imaged and measured for each culture condition.

For aggregation assays, individual aggregates from hanging drops were collected and five aggregates per condition were pooled into 500 μL of standard fibroblast culture medium in 24 well plates and incubated for 24 h at 37°C, 5% CO_2 with agitation on a shaker at 80 rpm. The number of cell aggregate fusion events was then scored.

Single nucleus RNA sequencing and data processing

Week 14 estimated gestation age skin was collected from two specimens from dorsal and ventral digits and from the back, snap frozen on dry ice, then stored at −80°C. Dermatoglyph developmental stage was assessed on the contralateral hand. For isolation of nuclei, frozen tissue was minced on ice in EZ Nuclei Lysis Buffer (Sigma-Aldrich) with 0.2 U/μl RNase inhibitor (Promega) and homogenized using a Polytron homogenizer for 7 s, then a Dounce homogenizer. Homogenates were filtered through 70 μm cell strainer, centrifuged at 500 g, then washed with EZ Nuclei Lysis Buffer with 0.2 U/μl RNase inhibitor followed by 1% BSA and 0.2 U/μl RNase inhibitor in PBS.

Libraries were prepared using a 10X Genomics Chromium Next GEM Single Cell 3′ Reagent Kit v3.1 following manufacturer instructions. Briefly, where possible 20,000 FACS sorted nuclei were loaded for each ventral, dorsal and back sample. cDNAs were amplified for 12 cycles and, based on their concentrations, sample index PCRs were performed for between 14 or 15 cycles. Sequencing was performed on the NextSeq 2000 platform (Illumina Inc, #SY-415-1002) using the NextSeq 1000/2000 P3 Reagents (100 cycles) v3 Kit (Illumina). Libraries were pooled in equimolar quantities and PhiX Control v3 (Illumina) library was spiked into the run at a concentration of ~1%. Numbers of paired end reads passing quality filters were 415 M and 506M (ventral digit skin), 442 M and 388 M (dorsal digit skin) and 463 M, 393M and 370M (back skin).

Unless stated otherwise, all processes below were carried out using default parameters. Reads were aligned to the human reference genome (GRCh38) pre-built (version 2020-A; provided by 10x Genomics) using the count function in Cell Ranger (10x Genomics; version 6.0.2; –include-introns –expect-cells = 10,000), and the resultant files in the "filtered_feature_bc_matrix" folder were imported to R (version 4.1.1) for downstream analysis through Seurat (version 4.0.5).[59,60]

The functions described below are from Seurat, unless stated otherwise. Seurat objects were converted to SingleCellExperiment[61] objects when required for compatibility with additional analytic tools. Cells defined as outliers by isOutlier from scater[62] (version 1.22.0) or that failed quality control thresholds were removed from further analysis; the hard lower/upper thresholds for number of features, number of counts, and globin percentage were 300/8000 and 1000/50,000 and $\geq$0.4% respectively. Doublets were removed using ScDblFinder[63] (version 1.8.0), followed by correcting for contaminant gene expression using DecontX[64] from celda (version 1.10.0) for each sample.

Integration of samples was done in two stages. First, a cluster of globin-contaminated cells were identified and removed, the remaining cells were split by sample and reintegrated as the final integration. In the integration steps, the following processes were carried out: FindVariableFeatures, SCTransform (initial integration; normalisations.methd = "SCT" and PrepSCTIntegration were used in the subsequent parameters) or ScaleData (final integration), SelectIntegrationFeatures (nfeatures = 3000 for the final integration), pFindIntegrationAnchors, and IntegrateData. Cell cycle status (defined by CellCycleScoring using "cc.genes.updated.2019" provided by Seurat) was regressed in both integration steps, and percentage globin was regressed out in the final integration step. Clustering was made on this initial integrated dataset through RunPCA, FindNeighbors and FindClusters (resolution = 0.5 and 0.3 for the initial and final integration, respectively). FindNeighbors was carried out using the first PC that exhibited cumulative percent greater than 90% and <5% associated variation. After the final integration, FindSubCluster was used on the basal and suprabasal keratinocyte cell populations resulting in clusters BKI, BKII, SKI and SKII. BKI consists of two cell clusters which we combined. UMAP (Uniform Mani-fold Approximation and Projection) was used to visualize the clusters using RunUMAP (features = VariableFeatures(x), min.dist = 0.5, seed.use = 1, n.neighbors = 15). Statistical tests were made using FindMarkers (test.use = "MAST").

Pseudotime analysis was carried out for the ventral digit and back samples for basal keratinocyte populations (clusters BKI and BKII) and specific fibroblast populations (FbI and FbII). Cells were subsetted and reintegrated using the SCT method described above, with cell cycle score and percentage globin regressed out. In the case of the basal keratinocyte population, cells with $\geq$3.5% ribosomal content were removed, and the k.param setting for FindNeighbors was set to 5. RunPHATE (k = 8, npc = 50, seed.use = 1 for the basal keratinocyte population; k = 10, seed.use = 1 for the dermal condensate population) was performed for PHATE[65] dimensional reduction. The cell embedding from PHATE was used for visualization in both these cell populations and for pseudotime trajectory analysis of the fibroblasts. Pseudotime trajectory inference was carried out with Slingshot[66] using the default setting for the fibroblast populations. General additive model (GAM) was used to identify temporally dynamic genes by exploring relationships between gene expression and pseudotime through negative binomial noise distribution models. The top 500 genes with significant ($p < 0.001$) relationship with pseudotime were kept for further analysis.

For visualizing the change in gene expression over pseudotime in basal keratinocytes, the back and ventral digit BKI and BKII cell populations were isolated and PCA and Slingshot analysis (clusterLabels = cell.population.annotation, end.clus = BKII, reducedDim = "PCA", allow.breaks = FALSE) were made on back and ventral samples independently. Cells in the sparse regions of the pseudotime trajectory were removed (i.e. if the nuclei frequency over 1/10th pseudotime-order were <25th percentile).

Identifying ridge and hair placode markers

To identify genes most strongly enriched in the dermatoglyph primary ridges and back hair follicles we sequentially compared differentially expressed transcripts between cluster BKI (unpatterned basal epithelium) and BKII (ridge/hair placode).

Comparison 1: Population BKII vs BKI from the same anatomical location (i.e. performed for both back and ventral digit samples) was compared to identify ventral ridge or hair placode markers. A uniqueness score (*U* score) was achieved by multiplying the Log2 FC (BKII vs BKI) x relative proportion of cells (pct. BKII/pct. BKI). Candidate genes with a *U* score over 3 were taken forward to Comparison 2. At this stage, non-protein coding and antisense RNAs were excluded, along with genes which had an adjusted p value of $p > 0.05$. To find uniquely differentially expressed genes between ventral digit ridges and hair placodes on the back, candidate genes from Comparison 1 were further analyzed in Comparison 2.

Comparison 2: Ventral digit BKII vs Back BKII. Candidate genes from Comparison 1 were further screened to remove those differentially expressed as a result of general epithelial gene expression differences between the back and ventral digit skin (ventral digit BKI vs Back BKI, genes with >0.5 Log 2 FC fold in the direction of the comparison). Of the remaining genes, those with a *U* score

(Log2 FC (ventral digit BKII vs back BKII, and vice versa) x relative proportion of cells (pct. Ventral digit BKII/pct. back BKII, and vice versa; if a gene was uniquely expressed it was given a relative proportion of 100) over 10 were deemed to be digit ridge or hair placode specific genes.

Atomic force microscopy

To prepare samples for atomic force microscopy (AFM) cross sectioning, fetal tissue was frozen in OCT and maintained at −80°C until sectioning. Cryosections were cut at 20 μm and adhered to Super-Frost Adhesion slides (Epredia) and maintained at −80°C until measured. Tissue was stained for K14 followed by incubation with an Alexa Fluor 488 conjugated secondary antibody. All staining was carried out in PBS containing 5% goat serum and cOmplete protease-inhibitor cocktail (Sigma-Aldrich).

All AFM experiments were carried out using a JPK NanoWizard III (Bruker) mounted on a Zeiss Axio Observer inverted microscope. Force indentation experiments were performed using a silicon nitride cantilever (Arrow-TL) modified with a 5 μm bead (micro-Particles GmbH). Thermal calibrations were performed before each experiment to determine the spring constant before use, with a nominal value of 0.3 N/m. Samples were maintained in PBS throughout measurement. Brightfield and K14 staining were captured using a standard fluorescein isothiocyanate (FITC) filter cube and used to align the cantilever to the sample. AFM Force maps were taken in 100 × 100 μm square grids, with a 100 x 100 pixel resolution. A cantilever deflection setpoint of 2 nN and indentation rate of 20 μm/s was used to gain the elastic properties. Force-distance curves were analyzed using the Hertz model modified for a spherical indenter using JPK data analysis software.

Skin organoids

Skin organoids were differentiated from the desmoplakin-mEGFP human iPSC line (Allen Institute for Cell Science, Coriell Institute) following published protocols.[38] After day 12 organoids were maintained with agitation at 80 rpm.

To assess proliferation, day 33 organoids were cultured for 24 h at 37°C, 5% CO_2 in 500 μL organoid maturation media[38] supplemented with recombinant human WNT3A (125 ng/mL, R&D Systems), recombinant human RSPO2 (250 ng/mL, R&D Systems), recombinant human/mouse/rat BMP2 (250 ng/mL, R&D Systems) or FH535 (5 μM, Sigma-Aldrich), alone or in combination. Vehicle (4 μM HCl 0.1%BSA, DMSO) controls were used as appropriate. For the final 2 h of culture the medium was supplemented with 10 μM EdU. Following treatment, organoids were fixed in 4% PFA and cryoembedded in 15% sucrose/7.5% gelatin.

10 μm cryosections underwent EdU detection and immunofluorescent staining for GFP as described above. Stained sections were imaged using a Zeiss LSM 880 confocal microscope. DAPI and EdU cells were counted in the basal layer of GFP+ve epidermis.

Ex vivo skin culture, treatment and qPCR

Dissected fetal volar skin samples were incubated on methylcellulose filters (Millipore) at 37°C, 5% CO_2 in DMEM containing 5% FBS and either control (vehicle), recombinant human WNT3A (250 ng/mL, R&D Systems) + recombinant human RSPO2 (500 ng/mL, R&D Systems), or recombinant human/mouse/rat BMP2 (500 ng/mL, R&D Systems). Samples were collected after 24 h and RNA was extracted using Tri-Reagent (Sigma-Aldrich) according to manufacturer's instructions. cDNA was synthesised using Superscript III Reverse Transcriptase (Invitrogen) with random primers (Promega). qRT-PCR reactions were carried out in 20 μL using SYBR Green Universal Master Mix (Roche) including Rox reference dye. Each reaction was performed in triplicate. For pulse chase experiments, fetal volar skin samples were cultured in DMEM/5% FBS containing 10 μM EdU for 2 h, followed by replacement with medium lacking EdU for the chase period.

Wavelet analysis of pre-pattern

Microscopy images with *EDAR in situ* hybridisation signal and K14 immunofluorescence were segmented to extract the upper and lower tissue sections and the segmented image used to create a mask. A central line was fitted to the masked image and 200 consecutive windows were placed angled perpendicular to the central line. The mask permits extraction of signal counts only within these windows. Raw signal was normalized by the highest count over all the windows and smoothed using a moving mean calculated over a sliding window of length 5 across neighboring data points. The results were robust to small changes in this window size and number of windows used. The amplitude of the spatial frequencies is informative as to their dominance in the observed signal. Amplitudes that are significantly larger than background denote non-random signal. The extracted signal information was decomposed using a generalized Morse wavelet basis.[67] The wavelet decomposition was applied using the "cwt" function in MATLAB.[68] All image preparation and analysis was performed in MATLAB.

Mathematical simulations

The mathematical model was based on a modified Gierer-Meinhardt reaction-diffusion system with saturation to allow for stripe formation.[69] Initial and boundary conditions were used to perturb the homogeneous steady state and initiate ridge formation. The model was solved using the commercial finite-element software COMSOL Multiphysics following a standard method to discretize the partial differential equations on the surface of a hemicylinder.[70] COMSOL files used are available (see key resources table).

QUANTIFICATION AND STATISTICAL ANALYSIS

Unless stated otherwise Fiji[57] was used for image analysis and measurement. Graph production and statistical analysis was performed using Graphpad Prism 9, statistical tests used are named in the figure legends.

Primary ridge wavelength measurements

Images of H&E stained digits on which the entire distal phalanx could be seen were used to measure interridge spacing (pattern wavelength). The length of the phalanx was measured from the distal tip to the joint between the distal and the medial phalanges, and interridge distance measurements made manually from ridge center to ridge center. Sections of digits 2, 3 and 4 were used for wavelength measurements.

Structural analyses

Immunofluorescent images of α-catenin and K14 stained ventral and dorsal digit sections from weeks 12–19 EGA were analyzed using Tissue Analyzer.[58] Cells were segmented, then structurally analyzed, including their degree of stretch and orientation, with respect to the x-y coordinates of the image. Cells were grouped into basal and suprabasal epithelium in both the ventral and dorsal samples, as well as the intermediate layer (defined as K14+ve non-basal epithelial cells) in the ventral samples only.

Single z stack images containing basal or suprabasal cell layers of stained whole mount ventral and dorsal digit samples were analyzed and segmented. Fabric tensor analysis was employed to quantify the planar orientation and anisotropy of structural morphology of the basal layers.[71] The method of mean intercept length (MIL) was used and all the calculated MILs were illustrated as a point cloud, representing the anisotropy of the cell. The point cloud was then fitted by an ellipse in MATLAB and the degree of anisotropy (DA) was calculated as $1D_1/D_2$, where D_1 and D_2 ($D_1 \leq D_2$) are two eigenvalues of the fitted ellipse. The cells are fully isotropic when DA = 0 and fully anisotropic when DA = 1.

Cell density and proliferation quantification

Cell counts were carried out using Fiji software on immunofluorescent images of sectioned digits and back skin stained with Ki67 and counterstained with DAPI. Images were taken using a Zeiss LSM 880 confocal microscope, a Zeiss LSM 710 confocal microscope, and a Leica DMLB upright fluorescent microscope. Images were taken at x20 magnification. Counts were taken from the entire field of view encompassing 300–600 μm linear skin length. Hair follicle structures were not included.

For mesenchymal cell counts, DAPI and Ki67 positive nuclei were counted to a depth of 40 μm from the basal epidermis. In samples with primary ridges the upper limit of the counted area was up to the basal cells in the interridge region.

For epithelial cell counting, the epithelium of samples with ridges was segregated into four different populations of K14+ve cells: basal ridge cells, basal interridge cells, suprabasal core ridge cells, and suprabasal cells. Basal and interridge populations were measured as a length (1 dimension) while suprabasal and dermal populations were measured as an area (2 dimensions). DAPI+ve nuclei and Ki67+ve nuclei were counted separately for each population. For total epidermal density and proliferation measurements all DAPI+ve nuclei and Ki67+ve nuclei from both ridges and interridge regions were included.

Ridge morphology and proliferation analysis

Ridge depth was measured from the deepest point of epithelium within the mesenchyme to the epithelial-mesenchymal junction at the interridge region. Ridges were separated into the bottom 20 μm (vertical height) and the remainder of the ridge, with DAPI+ve nuclei and Ki67+ve nuclei in the basal epidermis being counted separately for each zone. Individual ridge depths were measured and a mean taken for each image which was used to classify an image as below 20 μm or above 20 μm, permitting pairing of interridge and ridge measurements.

Mouse digit ridge analysis

Ventral images of toluidine blue stained adult forelimbs or TCF/Lef::H2B-GFP embryonic forelimbs were analyzed to assess ridge wavelength and thickness. For wavelength measurements, the distance between the central points of two ridges was measured on both the left and right hand side of a digit and this value averaged. For ridge thickness, the proximal to distal distance of each ridge was measured on both the left and right hand side of the digit and these measurements averaged. For each mouse, digits 3 and 4 were measured individually and averaged. We found no difference between the individual digit measurements.

For sweat gland measurements, forelimbs from 21-day-old *Egfr*$^{+/+}$ and *Egfr*$^{Wa5/+}$ mice were stained with toluidine blue and the number of sweat gland pores present on the digit ridges from digits 2–5 of blinded samples was measured independently by two scorers.

Flexion crease measurements

For measurement of cell density and proliferation, DAPI+ve nuclei and Ki67+ve nuclei were counted on tissue sections for 120 μm on either side of the deepest point of each crease. Ridge shape was assessed by measuring the width and depth of each ridge on tissue sections from the level of the bottom of the interridge basal cells. Ridge shapes were measured up to a distance of 500 μm from the deepest point of the metacarpophalangeal (MC) creases. The presence or absence of ridges was scored in the deepest part of each of the three digital flexion creases (DIC, PIC, MC) on H&E stained sections of digits; only flexion creases with clear ridges on both proximal and distal sides were included in this analysis. The depth of the suprabasal epithelium was measured at the deepest point of the crease and at 50, 100 and 150 μm from this point in both proximal and distal directions. Measurements were taken from the top of the basal layer in interridge regions and from an equivalent position in the ridges.

CellPress
OPEN ACCESS

Supplemental figures

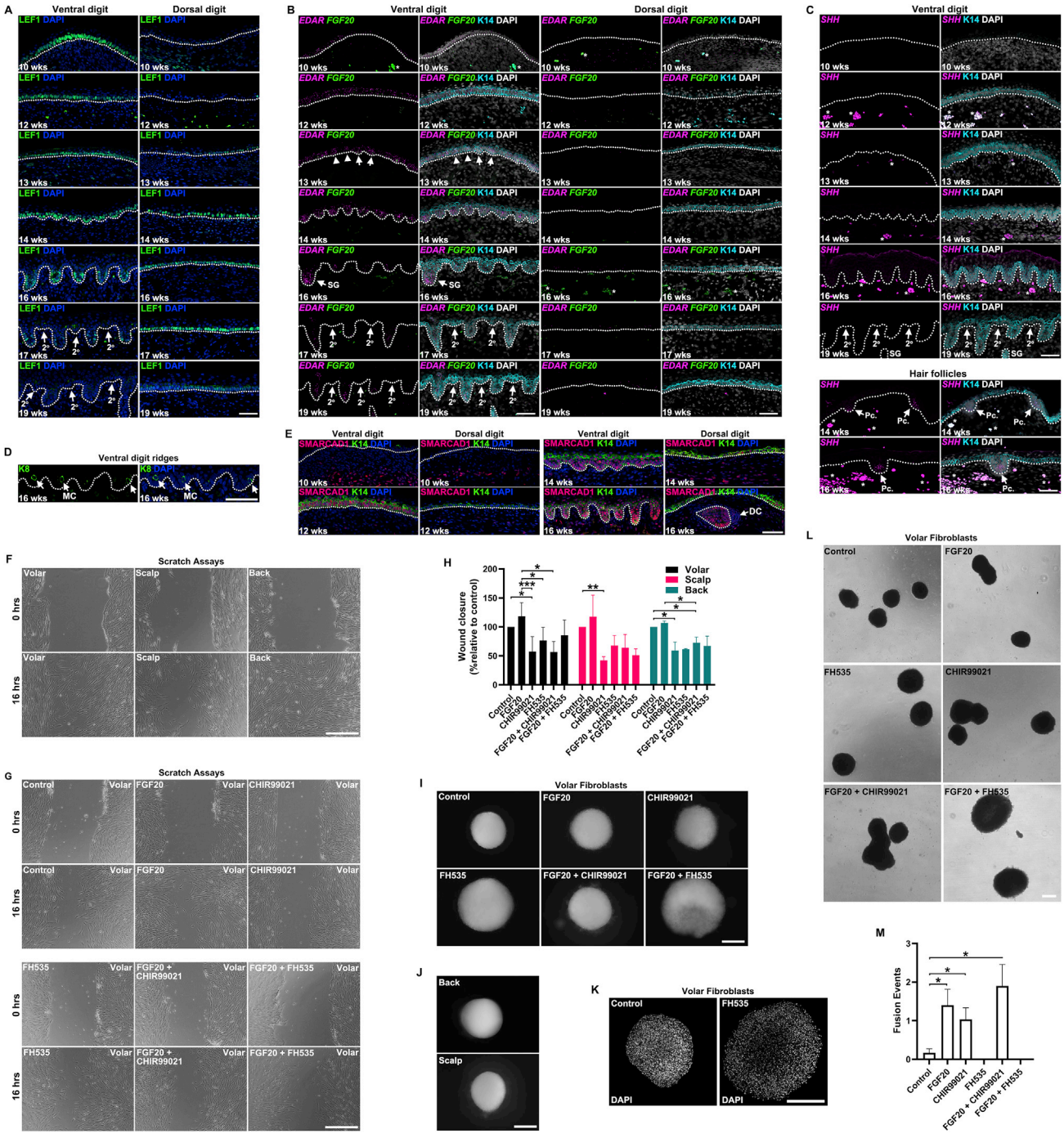

Figure S1. Timecourse of developmental gene and protein expression in dorsal and ventral digit skin, and WNT and FGF20 signaling promote cellular aggregation of fibroblasts, related to Figures 1 and 2

(A) Immunofluorescent detection of LEF1. Expression is widespread, then becomes intensified in the ridges. Ventral expression is earlier and stronger than dorsal. (B) *EDAR* and *FGF20* expression detected by RNAScope *in situ* hybridization. *EDAR* expression is widespread, then becomes intensified in the ridges and downgrowing sweat gland primordia. Ventral expression is earlier and stronger than dorsal. Neither *EDAR* nor *FGF20* are expressed in secondary ridges. At 13 weeks arrows indicate nascent ridges, arrowheads punctate *EDAR* expression.

(legend continued on next page)

(C) *In situ* hybridization detecting *SHH* expression in hair follicle placodes but not primary or secondary volar ridges at any age.
(D) KERATIN8 (K8) immunofluorescence confirms Merkel cell identification in the primary ridges.
(E) Immunofluorescent detection of SMARCAD1 expression. Greatest abundance is in volar epithelium and primary ridges.
(F) Representative images of scratch assays performed on fibroblasts derived from 12 weeks EGA scalp, back and volar skin.
(G) Representative images from scratch assays of volar fibroblasts treated with FGF20 (200 ng/mL), the GSK3β inhibitor CHIR99021 (5 μM) and the WNT/β-catenin pathway inhibitor FH535 (10 μM), alone or in combination.
(H) Quantification of wound closure at 16 h in scratch assays of volar, scalp and back fibroblasts. Error bars represent SEM of independent experiments (volar $n \geq 4$; scalp $n \geq 2$; back $n \geq 2$). *$p < 0.05$, **$p < 0.01$, ***$p < 0.001$ = Student's paired t-test.
(I) Representative images of volar fibroblast aggregates formed in hanging drop cultures after 48 h in control and experimental conditions modulating FGF and/or WNT signaling.
(J) Comparable aggregates form after 48 h in hanging drop cultures of fibroblasts derived from the back or scalp.
(K) Optical slices of aggregates stained with DAPI shows that inhibition of WNT signaling during hanging drop culture results in loosely formed cell aggregates.
(L) Following 48 h in hanging drop culture, five individual cell aggregates from each culture condition were pooled and allowed to interact for a further 24 h. Fusion is seen between aggregates from hanging drop cultures treated with FGF20 and/or CHIR99021 demonstrating altered cell surface and adhesive properties.
(M) Quantification of fusion events between individual aggregates formed under different hanging drop culture conditions. FGF20 and WNT/β-catenin stimulation promote aggregation, while inhibition of β-catenin transcriptional responses suppresses aggregation. Error bars represent SEM from at least five independent experiments. *$p < 0.05$ = Student's paired t-test. 2°, secondary ridge; DC, dermal condensate; MC, Merkel cell; Pc. hair placode; SG, sweat gland. Asterisks indicate examples of autofluorescent blood cells. Scale bars, 50 μm (A-E), 250 μm (F,G,I-L).

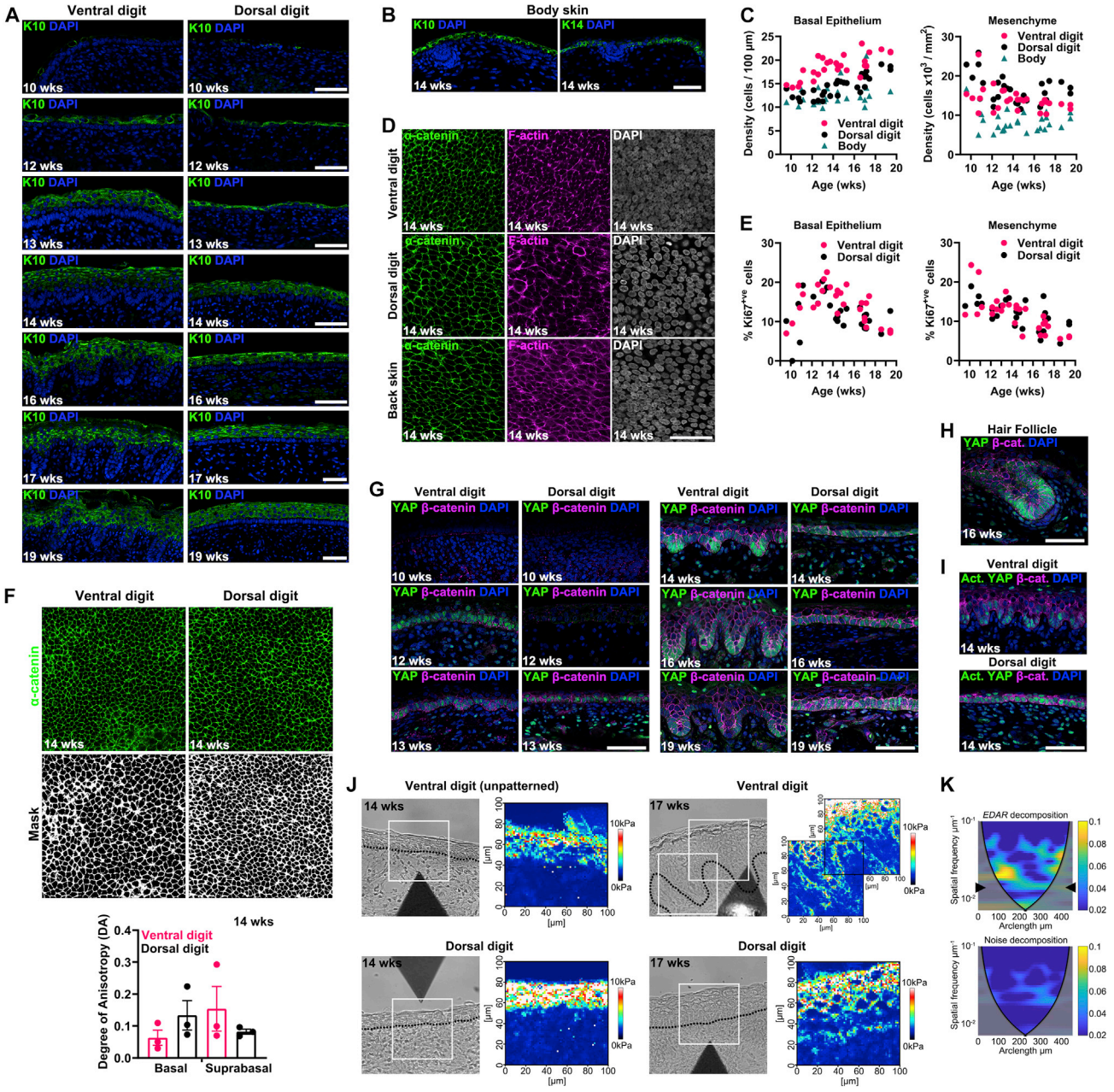

Figure S2. Differentiation and structure of human volar skin, related to Figure 3

(A and B) Immunofluorescent detection of KERATIN10 (K10) on (A) dorsal and ventral digit skin from 10 weeks to 19 weeks and (B) body skin at week 14. K14 detection is included for the body skin.

(C) Quantification of basal epithelial and mesenchymal cell density from weeks 10–19. Each data point represents an individual specimen. Ventral digit epithelium is more densely packed than that at other sites from week 12 to week 17, though by week 19 dorsal digit and body skin attain an epithelial density matching that of the volar skin at week 14, when the latter is producing primary ridges. Mesenchymal cell density is generally higher in the digit than on the body.

(D) z stack projection of basal epithelium from 14 weeks ventral digit, dorsal digit and back skin wholemount samples stained to detect α-catenin and F-actin, and counterstained with DAPI; increased basal cell density in the ventral digit is apparent.

(E) Quantification of Ki67+ve proliferative cells in basal epithelium and mesenchyme in dorsal and ventral digit skin. The fraction of cycling cells is not different between these sites, thus, a differential proliferation rate does not explain the increase in basal epithelial density on volar skin from week 12.

(F) (Above) Single z stack image of α-catenin stained basal epithelium of ventral and dorsal digit, and the derived masks used for cell shape analysis (relates to anisotropy analysis of Figure 3). (Below) Quantification of degree of anisotropy of basal and suprabasal epithelium on ventral and dorsal digit skin. Each point represents data from analysis of an individual specimen. Error bars represent SEM.

(legend continued on next page)

(G and H) Immunofluorescent detection of YAP in (G) dorsal and ventral digit skin from week 10 to week 19 and (H) developing hair follicle on 16 weeks body skin. YAP abundance follows epithelial differentiation, with no distinction between emerging primary ridges and surrounding epithelium at week 13, but increased nuclear localization at later stages of both primary ridge and hair follicle downgrowth.

(I) Detection of the active form of YAP in ventral and dorsal digit agrees with nuclear localization of total YAP, being elevated at the base of 14 weeks primary ridges and detected in most dorsal epithelial cells.

(J) Atomic force microscopy derived force maps of (left) week 14 unridged ventral epithelium and corresponding dorsal digit epithelium. The dorsal digit epithelium lacks a clear gradient of stiffness from suprabasal to basal layers at this stage. (Right) Maps of 17 weeks mature primary ridges in ventral and dorsal digit skin. In both a soft basal layer between the suprabasal epithelium and the epithelial-mesenchymal junction (dotted line) is visible.

(K) Wavelet transformation of *EDAR* expression signal and epithelial structure (noise), defined by K14 immunofluorescence, to identify pattern and wavelength. Image analyzed is Figure 3J. The *EDAR* signal decomposition (above) identifies a major wavelength at 30–50 μm (contiguous band of color across the image, arrowheads) while the structural analysis (below) identifies no pattern on the same skin. The gray region shows where boundary effects become significant and the analysis is thus uninformative in this area. Scale bars, 50 μm.

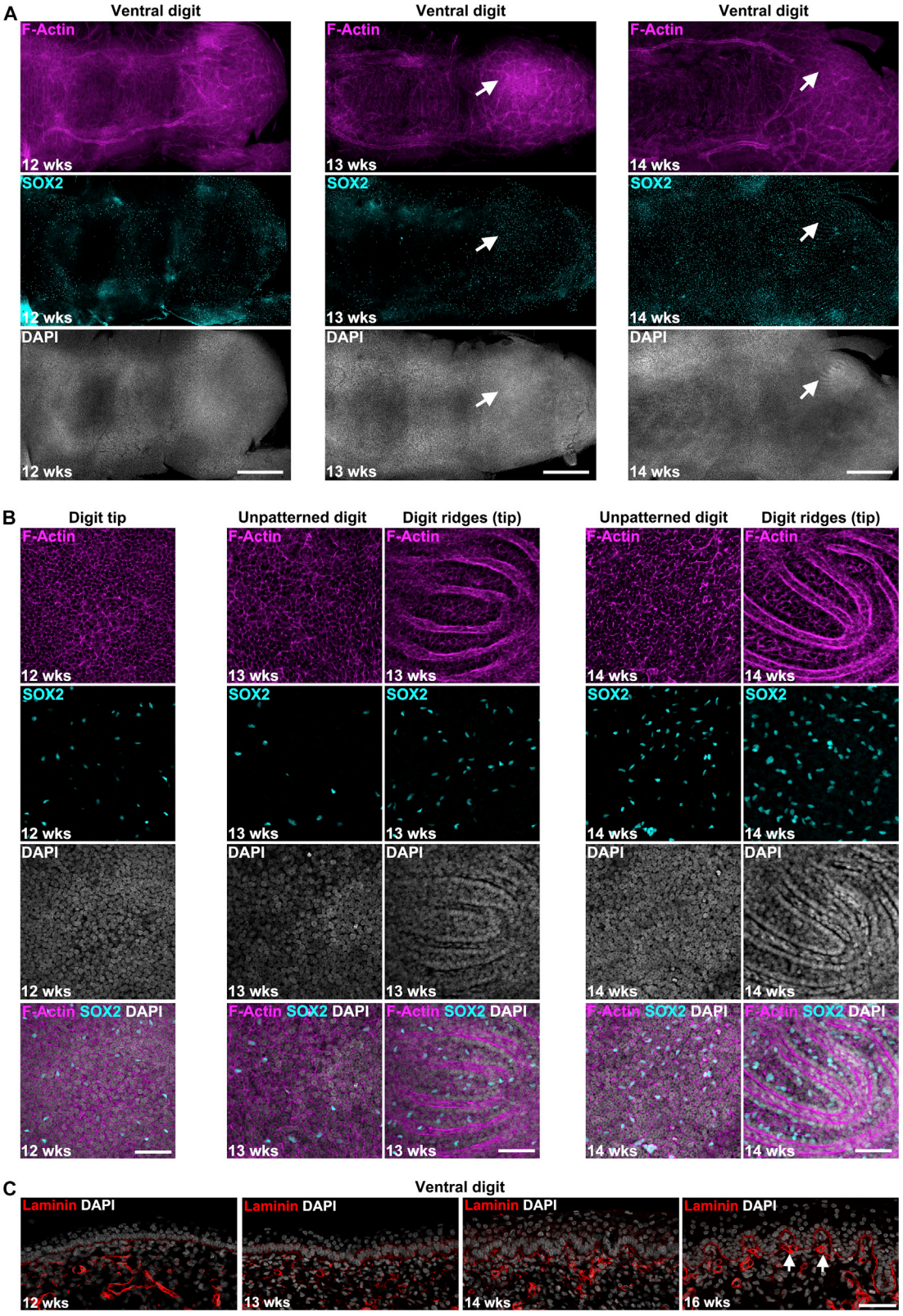

(legend on next page)

Figure S3. Absence of exogenous cellular templates for epidermal ridge patterns, related to Figure 3

(A) Arrangement of tissue structure, including vasculature, and Merkel cells revealed by phalloidin staining and SOX2 immunofluorescence on whole mounted ventral digit skin from weeks 12, 13 and 14, prior to and upon primary ridge formation. Neither tissue structure nor the arrangement of the initially dispersed Merkel cells prefigures the pattern of epithelial ridges, revealed by DAPI staining. Arrows indicate areas with ridges at the digit tip. Distal is to the right.

(B) Merkel cells, detected by anti-SOX2 immunofluorescence, become positioned within primary ridges after the ridges form and are not arranged in a periodic pattern prior to this.

(C) Immunofluorescent detection of basement membrane Laminin as a blood vessel marker. Blood vessels become aligned between primary ridges only after their downgrowth, at week 16, and blood vessel arrangement does not predict the emergence of the ridges at week 13. Scale bars, 500 μm (A); 50 μm (B, C).

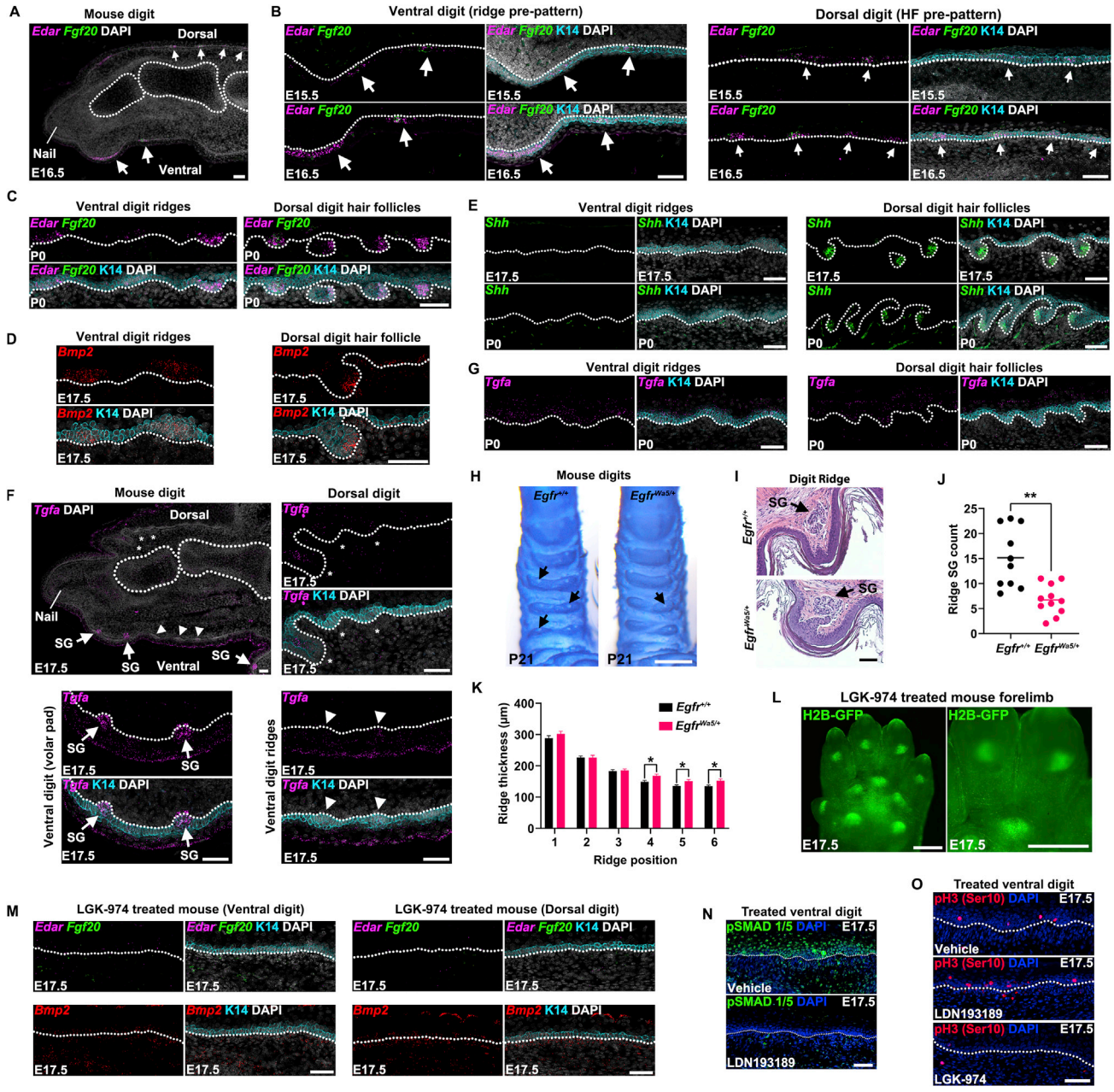

Figure S4. Gene expression, signaling and regulation in mouse transverse digit ridges, related to Figures 4 and 5

(A and B) RNAScope *in situ* hybridization detecting *Edar* and *Fgf20* expression (arrows) in mouse digits at E15.5 and E16.5 in the distal volar pad, and the proximal 2/3^{rds} of the ventral digit that produces transverse ridges. Focal *Edar* and *Fgf20* expression prefigure ridge emergence on the ventral digit skin, as they do for the hair follicle (HF) placodes emerging on the dorsal digit. The nail is indicated at the distal tip.

(C) As ridges and hair follicle placodes form histologically distinct structures in newborn (P0) skin, *Edar* and *Fgf20* expression, detected by *in situ* hybridisation, is intensified.

(D) *Bmp2* is expressed in both digit ridges and hair follicles.

(E) Lack of *Shh* expression in mouse transverse digit ridges, but clear expression in hair follicle epithelium, at E17.5 and P0.

(F) *Tgfa* expression in E17.5 mouse digit, showing expression in suprabasal epithelium, modest expression in early transverse ridges (arrowheads) and maturing hair follicles (asterisks), and intense expression in the sweat gland buds (arrows) that develop directly off the distal volar pad. The nail is indicated at the distal tip. SG, sweat gland.

(G) Expression of *Tgfa* in newborn transverse digit ridges and hair follicles. Stronger expression is detected in the ridges.

(H) Reduced EGFR signaling leads to a reduction in sweat glands (arrows) in digit ridges. Toluidine blue stained P21 mouse digits from wild type $Egfr^{+/+}$ and $Egfr^{Wa5/+}$ mutant mice, which carry the *Wa5* dominant negative *Egfr* allele containing a missense mutation (Asp833Gly) affecting the tyrosine kinase function of the receptor, resulting in diminished EGFR signaling.

(legend continued on next page)

(I) Cross sections of digit ridges confirming presence of sweat glands (SG) in both wild type and mutant mice. H&E stained.
(J) Quantification of sweat gland number in digit ridges from wild type and mutant mice. **$p < 0.01$ = Student's t-test.
(K) Quantification of digit ridge size in wild type and mutant mice. Error bars represent SEM from at least 10 individual mice per genotype. *$p < 0.05$ = Student's t-test. Ridge wavelength was not significantly changed between wild type and mutant mice (data not shown).
(L) Ventral view of E17.5 TCF/Lef::H2B-GFP forelimb, treated with WNT secretion inhibitor LGK-974 *in utero*. Transverse ridges are not observed.
(M) *In situ* hybridization fails to detect localized expression of transverse ridge markers *Edar*, *Fgf20* or *Bmp2* in LGK-974 treated embryos, demonstrating absence of the transverse ridges upon suppression of WNT activity. Hair follicle primordia on the dorsal side of the digit are also absent.
(N) Immunofluorescent detection of the BMP signal transducer phospho-SMAD1/5 in ventral digit skin of vehicle control and LDN193189 (BMP signaling inhibitor) treated E17.5 mouse forelimbs, confirming that BMP activity is supressed with inhibitor treatment.
(O) Immunofluorescent detection of the cell proliferation marker phospho histone H3 (Ser10) in vehicle control, LDN193189 and LGK-974 treated mouse forelimbs. Scale bars, 50 μm (A-G, I, M–O); 500 μm (H,L).

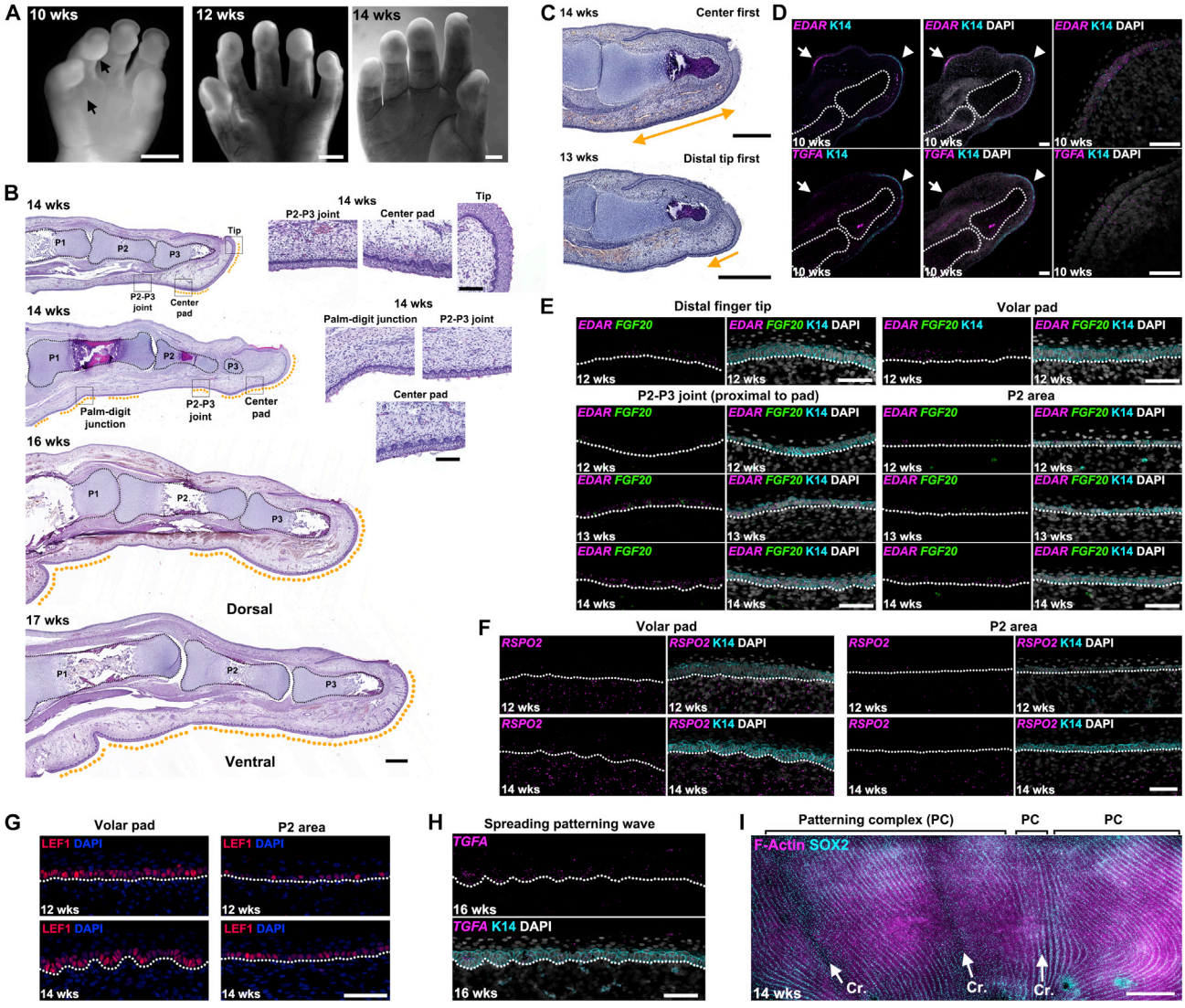

Figure S5. Fetal hand anatomy and primary ridge pattern initiation sites, related to Figure 6

(A) Images of entire hand at stages indicated. Volar pads are apparent at the distal third of the digits and select interdigital sites on the palm (arrows).

(B) H&E stained sections of digits at weeks 14–17 showing ridge initiation sites and spreading of ridge-forming waves. Boxed regions are enlarged at right. Uppermost week 14 digit shows pattern initiation at both the center of the volar pad and the digit tip. Orange dotted lines indicate regions with ridges.

(C) Distinction between digits which initiated patterning in the center of the volar pad (above) or at the distal tip (lower).

(D) Initiation of *EDAR* and *TGFA* expression at the center of 10 weeks volar pads (arrows). K14 expression initiates at the digit's distal tip (arrowheads).

(E) Expansion of *EDAR, FGF20* and K14 expression in basal epidermis and production of an intermediate layer (K14+ve suprabasal cells) from the distal tip across the digit from weeks 12–14.

(F) Stable expression of *RSPO2* in volar pad mesenchyme across weeks 12–14. On the medial digit *RSPO2* expression increases in this time period.

(G) LEF1 expression is strong in volar pads at weeks 12 and 14, and greater in the medial digit at week 14 than week 12, mirroring that of *RSPO2*.

(H) Expression of *TGFA* at the front of the ridge patterning wave.

(I) Whole mount visualization of ridge orientation on digit 5, detection of SOX2+ve Merkel cells and F-Actin (phalloidin stain). Cr. indicates the flexion creases. Three zones of contiguous ridge orientation (PC) are observed, demarcated above. Distal is to the right. Scale bars, 1 mm (A); 500 μm (B entire digit, C, I); 50 μm (B inset, E–H); 100 μm (D).

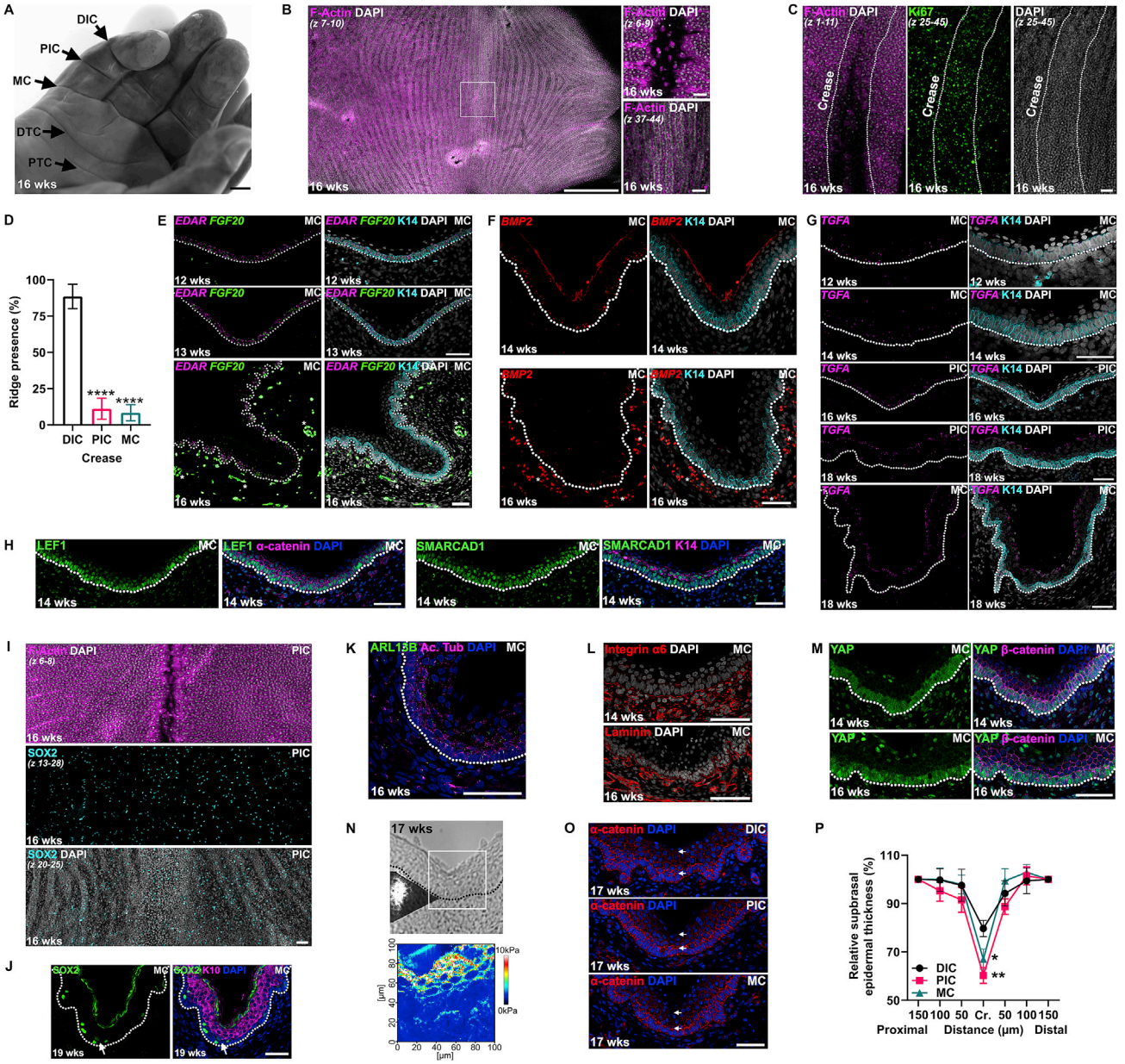

Figure S6. Structure, primary ridge arrangement, and molecular identity of flexion creases, related to Figures 6

(A) 16 weeks hand with flexion creases labeled. DIC, distal interphalangeal crease; PIC, proximal interphalangeal crease; MC, metacarpophalangeal crease; DTC, distal transverse crease; PTC, proximal transverse crease.

(B) Whole mount view of digit ventral skin stained with phalloidin (F-Actin) and DAPI, showing example of disordered primary ridges within a DIC, with parallel transverse ridges adjacent to the crease.

(C) Phalloidin and anti-Ki67 stained flexion crease (MC) lacking ridges but exhibiting broadly high proliferation within the crease.

(D) Frequency of histologically normal primary ridges detected within creases. The DIC carries morphologically normal ridges much more frequently than the PIC or MC. Error bars represent SEM from at least 9 independent flexion creases at each anatomical position. ****$p < 0.0001$ = ANOVA with pairwise comparisons.

(E) *EDAR* and *FGF20* expression across creases matches that of unpatterned skin at weeks 12 and 13, and that of the ridged skin surrounding the crease at week 16.

(F) *BMP2* expression is detected at the base of creases lacking histologically detectable ridges.

(G) *TGFA* expression is detected in flexion creases at the onset of and throughout ridge patterning, supporting the presence of cells with ridge identity within creases lacking morphological ridges. Mature suprabasal epidermis also expresses *TGFA*.

(H) LEF1 and SMARCAD1 are expressed normally across creases.

(I and J) SOX2 immunofluorescence demonstrates the presence and maintenance of Merkel cells within crease epithelium, as observed in the primary ridges. (I) z stack projection of stained wholemount week 16 ventral digit; (J) tissue section from a week 19 flexion crease. Arrow indicates Merkel cell presence in the crease.

(legend continued on next page)

(K) Epithelial cell polarity, indicated by apical localization of ARL13B and acetylated-Tubulin (Ac.Tub), is not disrupted at creases.
(L) Integrin α6 and Laminin detection indicates maintenance of the epithelial-mesenchymal junction at creases.
(M) YAP abundance and subcellular localization is unaltered at creases.
(N) Atomic force microscopy indicates suprabasal epithelium of normal stiffness, though thinned, at flexion creases.
(O) Immunofluorescent detection of α−catenin at the three digit flexion creases showing altered epithelial structure. Arrows illustrate suprabasal epithelial thickness.
(P) Quantification of suprabasal epithelial thickness at each of the three anatomical digit flexion creases. Error bars represent SEM from at least 9 independent flexion creases at each anatomical position from 16 weeks or older samples. *$p < 0.05$; **$p < 0.01$ = Mixed-effects analysis with pairwise comparisons. Cr. denotes the center of the crease. Error bars indicate SEM. Scale bars, 1 mm (A); 500 μm (B left); 50 μm (B right, C, E-M, O).